Journal of Asian Earth Sciences 191 (2020) 104215

Contents lists available at ScienceDirect

Journal of Asian Earth Sciences

journal homepage: www.elsevier.com/locate/jseaes

New insights into the hydrothermal evolution of skarn deposits: A case study of the Dongzhongla Pb-Zn deposit in Tibet, SW China

Guotao Sun[a,b], Jia-Xi Zhou[a,c,d,*], Kai Luo[a,b,d,e], Zhen-Zhong Xiang[d,e], Zhi-An Bao[f], Tao Sun[a,c]

[a] School of Earth Sciences, Yunnan University, Kunming 650500, China
[b] School of Ecology and Environmental Science, Yunnan University, Kunming 650500, China
[c] Key Laboratory of Sanjiang Metallogeny and Resources Exploration & Utilization, Ministry of Land and Resources, Kunming 650500, China
[d] State Key Laboratory of Ore Deposit Geochemistry, Institute of Geochemistry, Chinese Academy of Science, Guiyang 550081, China
[e] University of Chinese Academy of Sciences, Beijing 100037, China
[f] State Key Laboratory of Continental Dynamics, Department of Geology, Northwest University, Xi'an 710069, China

ARTICLE INFO

Keywords:
In situ trace elements of quartz
Fluid inclusions
C-O-S and in situ Pb isotopes
Hydrothermal evolution
Dongzhongla skarn Pb-Zn deposit
Tibet

ABSTRACT

Revealing hydrothermal evolution (from the early quartz-sulfide to the late fluorite-carbonate-sulfide stages) of skarn sulfide deposits is significant for understanding their ore formation processes, but the detailed studies are rare. In this study, we choose the Dongzhongla skarn Pb-Zn deposit (0.38 Mt Pb + Zn) located in central Lhasa, Tibet as a case study, and present detailed ore deposit geology and dataset of in situ chemical compositions of quartz, in situ Pb isotopic ratios of galena, sulfur isotopic compositions of sulfides and C-O isotopic compositions of hydrothermal calcite and wall rocks to address this issue. There are two types of hydrothermal quartz in the early stage: (1) the early phase euhedral quartz (Qz1) crosscut by quartz-sulfide veins, and (2) the late phase subhedral quartz (Qz2) coexisting with sulfides. TitaniQ thermometer of Qz1 and Qz2 limits the two phases with a temperature range of 336–427 °C (mean 373 °C) and 357–461 °C (mean 386 °C), respectively. The decreasing Al concentrations of Qz1 from core to rim suggest that magmatic fluids mixed with acidic meteoric water prevented the precipitation of sulfides during the early phase. The increasing Al and decreasing sulfur concentrations of Qz2 indicate that the increasing pH values of hydrothermal fluids made principal sulfides precipitate during the late phase. In addition, fluid inclusions and C-O isotopic studies reveal that the late stage minerals were deposited from low salinity (< 2 wt% NaCl equiv.) fluids at 250–300 °C. The rock/water (R/W) ratios for fluids were 0.2–1, whereas the water/rock (W/R) ratios for wall rocks were up to ~10. The $\delta^{34}S$ values range from 2.13 to 3.99‰, indicating a magmatic origin of sulfur. The Pb isotopic ratios are consistent with those of the early Cretaceous felsic intrusions and those of the Lhasa basement, suggesting that the source of Pb is associated with the early Cretaceous magmatism, which was generated by partial melting of the Lhasa basement. The in situ Pb isotopes also reveal that Pb derived from wall rocks can be negligible, although the W/R interaction accounts for the precipitation of sulfides. Hence, the hydrothermal evolution of the Dongzhongla skarn Pb-Zn deposit went through: (1) acidification process, i.e. magmatic fluids mixed with acidic meteoric water, which may restrain the precipitation of sulfides in the early phase, and (2) neutralization process, i.e. ore-forming fluids occurred at different degrees of W/R interaction during late phase, which is in favor of Pb-Zn mineralization.

1. Introduction

Skarn deposits are formed due to the degree of externally introduced/exchanged components (Einaudi et al., 1981; Meinert, 1992). The fluids involved in introduction/exchange process lead to variable textural characteristics and chemical compositions of minerals from skarn deposits. Hence, hydrothermal minerals formed in skarn systems record crucial metallogenic information (Harlov and Austrheim, 2013). Many researchers tried to decipher the geological history of skarn deposits through mineralogical/textural evidence by using refractory minerals, such as garnet (Gaspar et al., 2008; Xiao et al., 2018; Zhou et al., 2017) and magnetite (Huang et al., 2016; Liu et al., 2019; Nadoll et al., 2015; Zhao and Zhou, 2015). In addition, the compositional zoning patterns of garnet and magnetite were also used to reveal the evolution of hydrothermal fluids during the skarn stage (Zhai et al., 2014; Park et al., 2017). However, only a limited amount of research

* Corresponding author at: School of Earth Sciences, Yunnan University, Kunming 650500, China.
E-mail address: zhoujiaxi@ynu.edu.cn (J.-X. Zhou).

https://doi.org/10.1016/j.jseaes.2019.104215
Received 20 September 2019; Received in revised form 18 December 2019; Accepted 24 December 2019
Available online 27 December 2019

has been conducted to the minerals formed during the hydrothermal stage (from quartz-sulfide to carbonate stages), which impedes the understanding on the formation of Pb-Zn skarn deposits.

Quartz is another commonly zoned mineral, which can act as a chemical fingerprint for the skarn systems, especially for the quartz-sulfide stage. The textures and trace element signatures of quartz have been used to understand the evolution of fluids and provide information concerning the characteristics of fluids and water/rock (W/R) interaction (Allan and Yardley, 2007; Landtwing and Pettke, 2005; Rusk et al., 2006; Tanner et al., 2013). Additionally, the C-O isotopic compositions of hydrothermal calcite and related wall rocks place important constraints on understanding the precipitation temperatures of calcite and the ratios of W/R interaction (Levresse et al., 2004; Vazquez et al., 1998; Zheng and Hoefs, 1993).

In this study, we characterized the textures and in situ trace elements of quartz, and the C-O isotopic compositions of calcite and wall rocks from the Dongzhongla Pb-Zn deposit. In addition, we determined the factors that control the variations in trace elements of quartz, and the distinctions in C-O isotopes of calcite and wall rocks, and we also revealed the changes in physical and chemical conditions of hydrothermal fluids during W/R interaction. Furthermore, sulfur and Pb isotopes were employed to find out the sources of sulfur and metals, and in situ Pb isotopes were also conducted to determine the influx of metals during W/R interaction. The results provide new insights for understanding the hydrothermal evolution of skarn deposits.

2. Regional geology

The Himalayan-Tibetan Plateau is composed of the Himalayan, Lhasa, Qiangtang and Songpan-Ganze terranes from south to north. The Lhasa terrane, bordered by the Bangong-Nujiang suture (BNS) to the north and the Yarlung-Tsangpo suture (YTS) to the south, is further divided into the northern, central, and southern parts by the Shiquan River-Nam Tso Mélange Fault (SNMF) and the Luobadui-Milashan Fault (LMF) (Zhu et al., 2011) (Fig. 1a). The Lhasa terrane is composed of Precambrian basement, Paleozoic to Mesozoic marine strata, and arc-type volcanic rocks (Kind et al., 1996; Zhang et al., 2012, 2014). The Precambrian basement known as the Nyainqêntanglha Group, mainly consists of amphibolite facies (and locally, granulite facies) metamorphic rocks (Allégre et al., 1984; Pan et al., 2004; Zhu et al., 2013). The Precambrian basement is covered by the Carboniferous-Permian metasedimentary rocks, which in turn are covered by Jurassic-lower Cretaceous sedimentary rocks. All the cover sedimentary rocks contain volcanic rocks and abundant glacial-marine diamictites (Pan et al., 2004, 2006; Zhu et al., 2010, 2013).

Controlled by the complex tectonic evolution of the Neo-Tethys Ocean and Bangong-Nujiang Ocean, the Lhasa terrane has experienced the processes of southward subduction of the Bangong-Nujiang Ocean slab (Zhu et al., 2009, 2011), northward subduction of the Neo-Tethys Ocean slab (Yin and Harrison, 2000; Chu et al., 2006; Ji et al., 2009), the collision of Indian-Asian continents (Mo et al., 2005, 2007), and the E-W extension (Coleman and Hodges, 1995; Blisniuk et al., 2001; Williams et al., 2001). These processes were recorded by abundant magmatic rocks (Hou et al., 2004, 2009; Tang et al., 2010; Gao et al., 2011a), such as Cretaceous S- and I-type granites (143–110 Ma) (Zhu et al., 2009, 2011), and Cretaceous (137–80 Ma) (Zhu et al., 2009, 2011) and Paleocene–Eocene igneous rocks (65–51 Ma) (Gao et al., 2011b; Hou et al., 2012; Zhao et al., 2014), as well as Miocene porphyries (20–11 Ma) (Gao et al., 2011b; Yang et al., 2016; Sun et al., 2018).

In the Lhasa terrane, the economic deposits include porphyry Cu-(Mo-/Au) and Mo deposits, and skarn Fe-(Cu) and Pb-Zn-(Ag) deposits (Hou et al., 2009). Porphyry Cu-(Mo-/Au) deposits are mainly distributed in the southern part (Hou et al., 2009; Zeng et al., 2017; Sun et al., 2018), while porphyry Mo and skarn Pb-Zn-(Ag) deposits are distributed in the central part (Wang et al., 2015, 2016; Sun et al., 2017). Skarn Fe-(Cu) deposits are distributed at the southern margin of the central part (Zheng et al., 2015). Among these deposits, the skarn Pb-Zn-(Ag) deposits are an important ore type in the studied region.

The Dongzhongla-Sharang Pb-Zn-(Ag)-Mo ore field, located in the eastern part of the central Lhasa (Fig. 1a), consists of one porphyry Mo deposit (Sharang) and four skarn Pb-Zn-(Ag) deposits (i.e. Dongzhongla, Yaguila, Dongzhongsongduo and Zhawa) (Fig. 1b). In this ore field, the exposed strata are the NE-trending Lower Ordovician Songduoyan Formation, Upper Carboniferous Laigu Formation, Middle Permian Luobadui Formation and the Paleocene Napa Formation (Fig. 1b). Magmatic rocks of different ages were identified (Fei et al., 2010b; Zhao et al., 2015; Gao et al., 2017), including 128–124 Ma quartz/granite porphyries, 69–66 Ma and 53–51 Ma granite porphyries, and 22–18 Ma dykes. The Mo deposit formed at 52.3 Ma has genetic association with the *syn*-collision I-type granite porphyries (Zhao et al., 2014, 2016). The skarn Pb-Zn-(Ag) deposits occurred along the contact zones between granite porphyries and carbonate rocks formed in different ages, for example, Cretaceous (e.g. Dongzhongla, ~124 Ma, Fu et al., 2017) and Paleocene (e.g. Yaguila, ~65 Ma, Gao et al., 2011b).

3. Geology of the Dongzhongla deposit

3.1. Ore deposit geology

The Dongzhongla deposit is hosted in the Middle Permian Luobadui Formation limestone and calcareous slate (Fig. 2a). The lower section of the Luobadui Formation mainly consists of calcareous slate, while the upper section is dominantly composed of limestone. Pb-Zn ore bodies are hosted by limestone of the upper section. The geological structures in the Dongzhongla ore district are characterized by overturned anticlines and inter-layered fracture zones in limestone of the upper section with a NE-trending direction (Fei et al., 2018).

Granite porphyry, quartz porphyry and diorite porphyrite are mainly intrusive rocks in the mining area, which have zircon U-Pb ages of 124 Ma (Fei et al., 2010b), 127 Ma (Cui et al., 2011), and 117 Ma (Fei et al., 2010d), respectively.

Four ore bodies (Nos. I, II, III, and IV) are recognized in this deposit, of which No. I is the largest. No. I ore body is located in the eastern part of the mining area, with a length of approximately 500 m and an average thickness of approximately 20 m. This ore body is dipping at an angle of 50°–70° toward 155° (Fig. 2b), with strata-bound or lenticular shapes. The ores are mainly massive, veined, banded, or disseminated (Fig. 3).

3.2. Mineralogy

The ore minerals are mainly sphalerite, galena, chalcopyrite, pyrrhotite, and pyrite (Fig. 4a–d). The gangue minerals mainly include actinolite, diopside, quartz, fluorite, and calcite (Fig. 4d and f).

Two generations of quartz (Qzl and Qz2) were recognized. Qz1 is disseminated in wall rocks and occurs as euhedral crystals with sizes of 0.3–2 cm (Figs. 3e, f and 4e). There are no sulfides coexisting with Qz1 (Fig. 3e, f). Qz2 has subhedral crystals with sizes of 0.1–1 cm and coexists with sulfide veins that crosscut the Qz1 crystals (Fig. 3e, f).

In addition, two generations of sphalerite (Sp1 and Sp2) and galena (Gn1 and Gn2) were recognized. The Sp1 and Gn1 coexist with Qz2, all of which jointly formed massive, banded or veined sulfide ores. Parts of Qz2-Sp1-Gn1 veins crosscut skarn and wall rocks (Fig. 3a, e). The Sp2 and Gn2 coexist with fluorite and calcite, forming ore veins together, which often crosscut skarn and Qz2-Sp1-Gn2 ores (Figs. 3d and 4f).

3.3. Mineral paragenesis and stages

The mineral paragenesis can be divided into skarn, quartz-sulfide, and fluorite-calcite-sulfide three stages (Fig. 5). The skarn stage is characterized by a mineral assemblage of actinolite and diopside

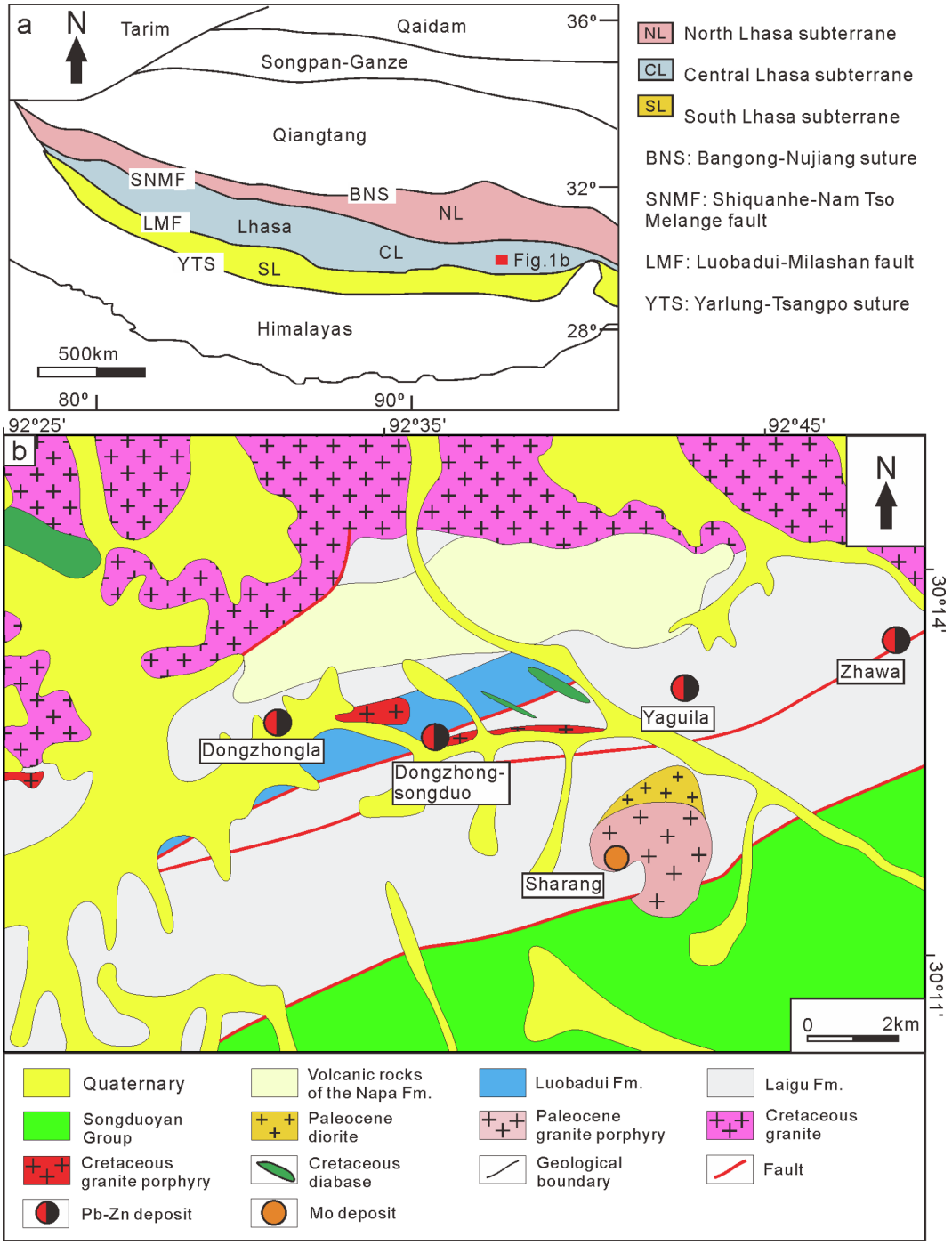

Fig. 1. Regional geology maps of the study area. (a) Map of the Himalayan-Tibetan Plateau, showing tectonic divisions (after Zheng et al., 2015). (b) Geological map of Dongzhongla-Sharang region showing the location of major deposits (after Gao et al., 2011a).

(Figs. 3a, b and 4f). The quartz-sulfide stage can be divided into an early phase that is composed of Qz1 without sulfides (Fig. 3e, f), and the late phase that consists of subhedral Qz2 and Sp1, Gn1, chalcopyrite, pyrrhotite, and pyrite. The minerals of fluorite-calcite-sulfide stage are mainly fluorite, calcite, Sp2, and Gn2 (Figs. 3d and 4e, f).

3.4. Wall rock alteration

Skarns are the most important alteration type in the Dongzhongla deposit (Fig. 3a), followed by silicification and carbonation. Skarn minerals are mainly diopside and actinolite (Fig. 3b, d), which occur along the contact zone between granite porphyries and limestone of the Luobadui Formation (Fig. 2b). Silicification is spatially adjacent to the wall rocks (Fig. 3b), and is dominated by disseminated Qz1 within wall rocks, and Qz2 veins crosscut skarn and wall rocks (Fig. 3e, f). Carbonation is mainly composed of calcite, which together with fluorite are also observed crosscutting skarn (Fig. 3d). The Pb-Zn mineralization is mainly associated with the silicification and carbonation (Fig. 3d–f).

4. Samples and method

Samples for textural, chemical and isotopic analyses were collected from underground tunnels (e.g. 5130 m and 5160 m) of the Dongzhongla deposit. Reflected microscopy was used to characterize

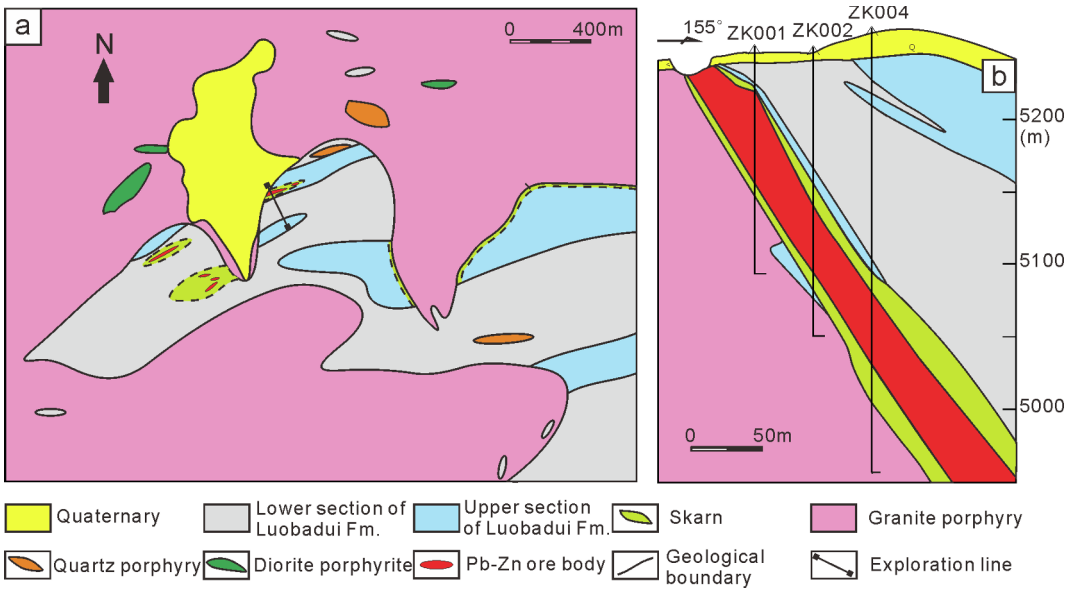

Fig. 2. Geological map of the Dongzhongla Pb-Zn deposit. (a) Geological map of the Dongzhongla Pb-Zn deposit. (b) Cross section of the Dongzhongla Pb-Zn deposit.

the sulfide assemblages of the Dongzhongla deposit. Quartz grains from sample DZL-29 were mapped in detail using CL images. Based on the CL images, LA-ICPMS was used to analyze in situ trace elements compositions of quartz. Seven calcite samples from fluorite-calcite-sulfide stage and five limestone bulk-rock samples were used for C-O isotope analysis. Nine sulfide samples from quartz-sulfide stage were analyzed for sulfur isotopic compositions. Ten galena samples from quartz-sulfide stage were analyzed for bulk Pb isotopic ratios. LA-MC-ICPMS was used to analyze in situ Pb isotopic ratios of Gn1 and Gn2.

4.1. Microthermometry and laser Raman spectroscopy

Microthermometric analysis of fluid inclusions was conducted at the Laboratory of Fluid Inclusions, State Key Laboratory of Ore Deposit Geochemistry (SKLODG), Institute of Geochemistry, Chinese Academy of Science (IGCAS), Guiyang. The double-polished thin sections were observed under optical microscope, then representative fluid inclusions were selected for microthermometry using a Linkam THMSG 600 heating-freezing stage (−198 to 600 °C). Synthetic fluid inclusions were used to calibrate the stage to ensure the measurement accuracy. The precisions of freezing data and heating data are 0.1 and 2 °C, respectively.

Laser Raman spectroscopy analysis was performed at room temperature using an InVia Reflex confocal Raman microscope at the SKLODG, IGCAS. Laser power of 20 mW, spatial resolution of 1–2 μm, and integration time of 30 s were used during the analysis.

4.2. Cathodoluminescene (CL)

CL maps were conducted on a JSM-7800F scanning electron microscope equipped with a MonoCL4 spectrometer at the SKLODG, IGCAS, to image the internal structure of quartz crystals. Images were collected at a working distance of 14.1 mm and an accelerating voltage of 10 kV.

4.3. LA-ICPMS analysis

LA-ICPMS spot analysis of quartz was carried out at the SKLODG, IGCAS. Laser sampling was performed using an Agilent 7900 ICP-MS equipped with a GeoLasPro 193 nm ArF excimer laser. Laser repetition of 10 Hz, energy density of 12 J/cm^2 and spot size of 44 μm were used during the analysis. For the quantitative calibrations, external standard of NIST SRM610 and GSE-1G were used and analyzed twice every 10 analyses. An internal standard-in-dependent calibration strategy, which is based on the normalization of the sum of all metal oxides to 100 wt%, was applied to the calibrations (Liu et al., 2008). NIST SRM612 and GSD-1G were analyzed to monitor the accuracy of the results, which show that the uncertainties of most elements are less than 10%. A nature quartz standard was also analyzed to monitor the accuracy. This standard has recommended values for Ti (57 ± 4 ppm), Al (154 ± 15 ppm), Li (30 ± 2 ppm), Fe (2.2 ± 0.3 ppm), Mn (0.34 ± 0.04 ppm), Ge (1.7 ± 0.2 ppm) and Ga (0.020 ± 0.002 ppm) (Audétat et al., 2015). The detailed analytical procedures are described in Lan et al. (2017, 2018).

4.4. Carbon and oxygen isotope analysis

The $\delta^{13}C$ and $\delta^{18}O$ values were obtained by a Finnigan MAT-253 mass spectrometer at the SKLODG, IGCAS. Hydrothermal calcite separates and limestone samples were reacted with pure phosphoric acid to produce CO_2. The analytical precisions (2σ) are ± 0.3‰ for $\delta^{13}C$ values and ± 0.6‰ for $\delta^{18}O$ values. $\delta^{18}O_{SMOW} = 1.03086 \times \delta^{18}O_{PDB} + 30.86$ (Friedman and O'Neil, 1977).

4.5. Sulfur isotope analysis

Sulfur isotope analysis was undertaken at the SKLODG, IGCAS, by a Finnigan MAT-253 mass spectrometer. GBW 04415 and GBW 04414 Ag_2S were used as external standards, and the Vienna Canyon Diablo Troilite (V-CDT) was used as reference standard. The analytical precision is ± 0.2‰ for $\delta^{34}S$ values.

4.6. Lead isotope analysis

The bulk Pb isotopic ratios of galena were analyzed at the Radiogenic Isotope Facility, School of Earth Sciences, the University of Queensland, Brisbane. The analysis was conducted on a Micro-mass Isoprobe MC-ICPMS equipped with 12 adjustable Faraday collectors. Approximately 100 mg of galena was dissolved in HF for several hours in Teflon beakers. Pb from galena was purified in HBr-HCl media by double-pass over miniaturized anion-exchange columns. Purified Pb was dissolved in 1 ml of 2% HCl prior to final analysis. The details of Pb isotope analysis are similar to those reported by Collerson et al. (2002). The results for the standard NIST SRM981 are $^{206}Pb/^{204}Pb$ = 16.9405 ± 0.002 (2σ),

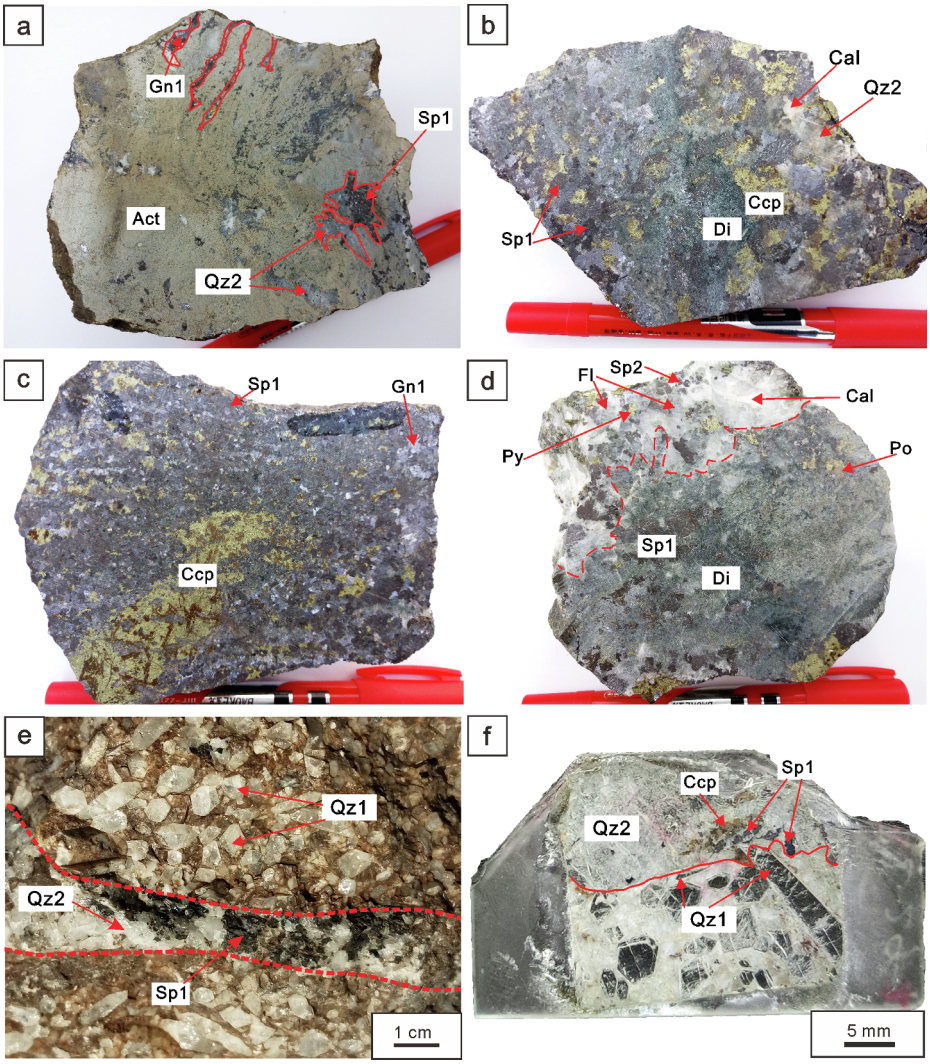

Fig. 3. Photographs illustrating the ore structure and main minerals of the Dongzhongla Pb-Zn deposit. (a) Quartz (Qz2)-sulfide veins crosscut skarn; (b) Massive ore with sphalerite, chalcopyrite and galena, showing residual diopside and hydrothermal quartz, calcite; (c) banded ore with sphalerite, chalcopyrite and galena; (d) Skarn minerals replaced by sulfide, and in turn crosscut by fluorite and calcite; (e) Qz2-sulfide vein crosscut early euhedral quartz (Qz1); (f) Photograph of thin section showing Qz2-sulfide veins crosscut euhedral Qz1. Act, actinolite; Di, diopside; Sp, sphalerite; Gn, galena; Ccp, chalcopyrite; Qz, quartz; Cal, calcite.

$^{207}Pb/^{204}Pb$ = 15.4943 ± 0.0007 (2σ) and $^{208}Pb/^{204}Pb$ = 36.7171 ± 0.0019 (2σ). These values are consistent with the reported reference values (Galer and Abouchami, 1998).

In situ Pb isotope analysis was conducted on a Nu II MC-ICPMS equipped with a 266 nm NWR UP Femto femtosecond (fs) laser ablation system at the State Key Laboratory of Continental Dynamics, Northwest University, Xi'an. Analysis was performed in line mode using spot size of 9 μm, laser energy of 7 J/cm^2, laser frequency of 3 Hz and ablation way of 3 μm/s. Each analysis time consisted of 20-s background collection followed by 50-s laser ablation for signal collection. The Tl (20 ppb, NIST SRM 997, $^{205}Tl/^{203}Tl$ = 2.38890) and NIST SRM 610 glass were served as internal and external standards, respectively. The details of fs LA-MC-ICPMS in situ Pb isotope analysis were described by Chen et al. (2014) and Bao et al. (2016).

5. Results

5.1. Fluid inclusion study

5.1.1. Petrography and laser Raman spectroscopy

Fluid inclusions in fluorite are mainly aqueous type (Fig. 6a) and are two-phase (L_{aq} + V_{aq}) H_2O–NaCl inclusions (Fig. 6c). These inclusions have variable morphologies with sizes of 7–30 μm and V/L (volume/liquid) ratios of 0.3–0.5. Few inclusions have daughter crystals (Fig. 6b), which are calcite suggested by Laser Raman spectroscopy (Fig. 6d).

5.1.2. Microthermometry

Microthermometry results are listed in Supplementary Table 1 and are presented in Fig. 7. Fluid inclusions in fluorite yield T_{hTOT} of 195–250 °C (Fig. 7a) and have salinities ranging from 0.2 to 1.6 wt% NaCl equiv. (Fig. 7b).

5.2. Combining textures and trace elements of quartz

Trace elemental data for quartz are listed in Supplementary Table 2 and are presented in Figs. 8 and 9.

Qz1 exhibits an oscillatory banding in CL images (Fig. 8a). LA-ICPMS data reveal that aluminum (Al) is the most abundant trace element in Qz1, and its concentrations range from 41 to 1453 ppm. Qz1 also contains some other trace elements, such as Li, P, S, Ti, and Ge. The Al and Li are found to have a high correlation in quartz crystals (Fig. 8c), but their relationships with CL images are ambiguous.

The CL images of Qz2 show fine oscillatory banding with irregular

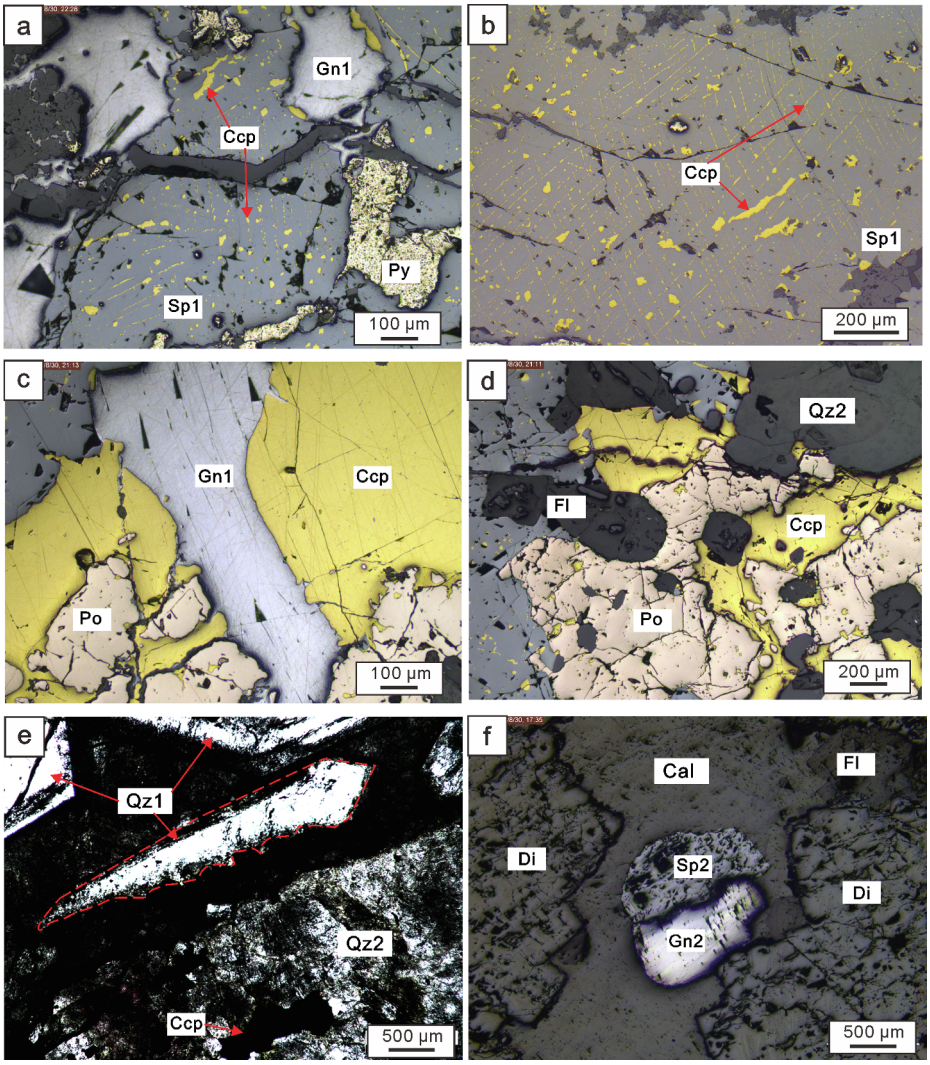

Fig. 4. Textural features of sulfides from the Dongzhongla Pb-Zn deposit. (a) Galena replacing sphalerite and chalcopyrite, quartz vein crosscut sphalerite (reflected light); (b) Chalcopyrite is present as net or irregular inclusions in sphalerite (reflected light); (c) Galena vein crosscut sphalerite, chalcopyrite and pyrrhotite (reflected light); (d) Fluorite replacing sphalerite, chalcopyrite, pyrrhotite and quartz (reflected light); (e) Qz2-sulfide vein crosscut euhedral Qz1 (transmitted light); (f) Fluorite-calcite-sphalerite-galena vein crosscut diopside (transmitted light). Di, diopside; Sp, sphalerite; Gn, galena; Ccp, chalcopyrite; Qz, quartz; Cal, calcite.

sub-crystals (Fig. 8b). Qz2 contains Al, S, P, Li, Na, Ti, and Ge. The concentrations of Al show great variance ranging from 5.18 to 637 ppm within a single crystal. Lithium (Li) distribution is correlated with that of Al (Fig. 8d). The relationship between Al (and Li) and CL intensity is irrelevant.

5.3. Carbon-Oxygen isotopic compositions

The $\delta^{13}C_{PDB}$ and $\delta^{18}O_{SMOW}$ values of hydrothermal calcite separates and limestone bulk-rock samples are listed in Table 1 and are shown in Figs. 10 and 11. Hydrothermal calcite has $\delta^{13}C_{PDB}$ and $\delta^{18}O_{SMOW}$ values ranging from −5.1 to 0.3‰ (mean −2.5‰) and 1.7 to 4.7‰ (mean 2.7‰), respectively. The $\delta^{13}C_{PDB}$ and $\delta^{18}O_{SMOW}$ values of fresh limestone are 2.3‰ and 19.8‰, while altered limestone samples have $\delta^{13}C_{PDB}$ and $\delta^{18}O_{SMOW}$ values ranging from −2.4 to 3.8‰ (mean 0.54‰) and 8.0 to 15.7‰ (mean 13.2‰).

5.4. Sulfur isotopic compositions

The $\delta^{34}S_{CDT}$ values of sulfides are listed in Table 2 and are presented in Fig. 12. The $\delta^{34}S_{CDT}$ values of all sulfide minerals are between 2.13 and 3.99‰ (mean 2.87‰), of which galena has $\delta^{34}S_{CDT}$ values ranging from 2.13 to 2.89‰ (mean 2.62‰), and the $\delta^{34}S_{CDT}$ values of sphalerite and pyrite are 3.99‰ and 3.53‰, respectively.

5.5. Lead isotopic ratios

Lead isotopic ratios of galena from the Dongzhongla deposit are listed in Supplementary Table 3 and are shown in Fig. 13. $^{206}Pb/^{204}Pb$, $^{207}Pb/^{204}Pb$ and $^{208}Pb/^{204}Pb$ ratios of bulk galena range from 18.635 to 18.640, 15.699 to 15.702 and 39.094 to 39.111, respectively. In situ Pb isotopic ratios of galena are $^{206}Pb/^{204}Pb$ = 18.634–18.644, $^{207}Pb/^{204}Pb$ = 15.701–15.710 and $^{208}Pb/^{204}Pb$ = 39.096–39.134, with $^{207}Pb/^{206}Pb$ = 0.8426–0.8428 and $^{208}Pb/^{206}Pb$ = 2.0981–2.0991.

6. Discussions

6.1. Sources of ore-forming elements

6.1.1. Source of sulfur

Sulfur minerals in the Dongzhongla deposit occur as sulfides, such as pyrrhotite, chalcopyrite, sphalerite, galena and pyrite, rather than sulfate. Hence, the $\delta^{34}S$ values of sulfides can approximately reflect those of ore-forming fluids (Ohmoto, 1972). Sulfides have $\delta^{34}S$ values

Minerals	Skarn	Hydrothermal stages	
		Quartz-sulfide	Fluorite-calcite-sulfide
Diopsite			
Actinolite			
Pyrite			
Sphalerite		Sp1	Sp2
Chalcopyrite			
Pyrrhotite			
Galena		Gn1	Gn2
Quartz		Qz1 Qz2	
Fluorite			
Calcite			

Fig. 5. Paragenesis of minerals from the Dongzhongla Pb-Zn deposit.

ranging from 2.13 to 3.99‰ (Fig. 12a), with a mean $\delta^{34}S$ value of 2.87‰, suggesting that the $\delta^{34}S$ values of ore-forming fluids are about 2–4‰. The basement mainly consists of metamorphic rocks, which have a larger range of $\delta^{34}S$ values from −20 to 20‰ (Seal, 2006) than those of sulfides. This means that the sulfur in ore-forming fluids could not be sourced mainly from the basement. In addition, the sediment sulfur of wall rocks has $\delta^{34}S$ values ranging from −9.0 to −8.6‰ (Wang et al., 2016), which are significantly lower than those of sulfides.

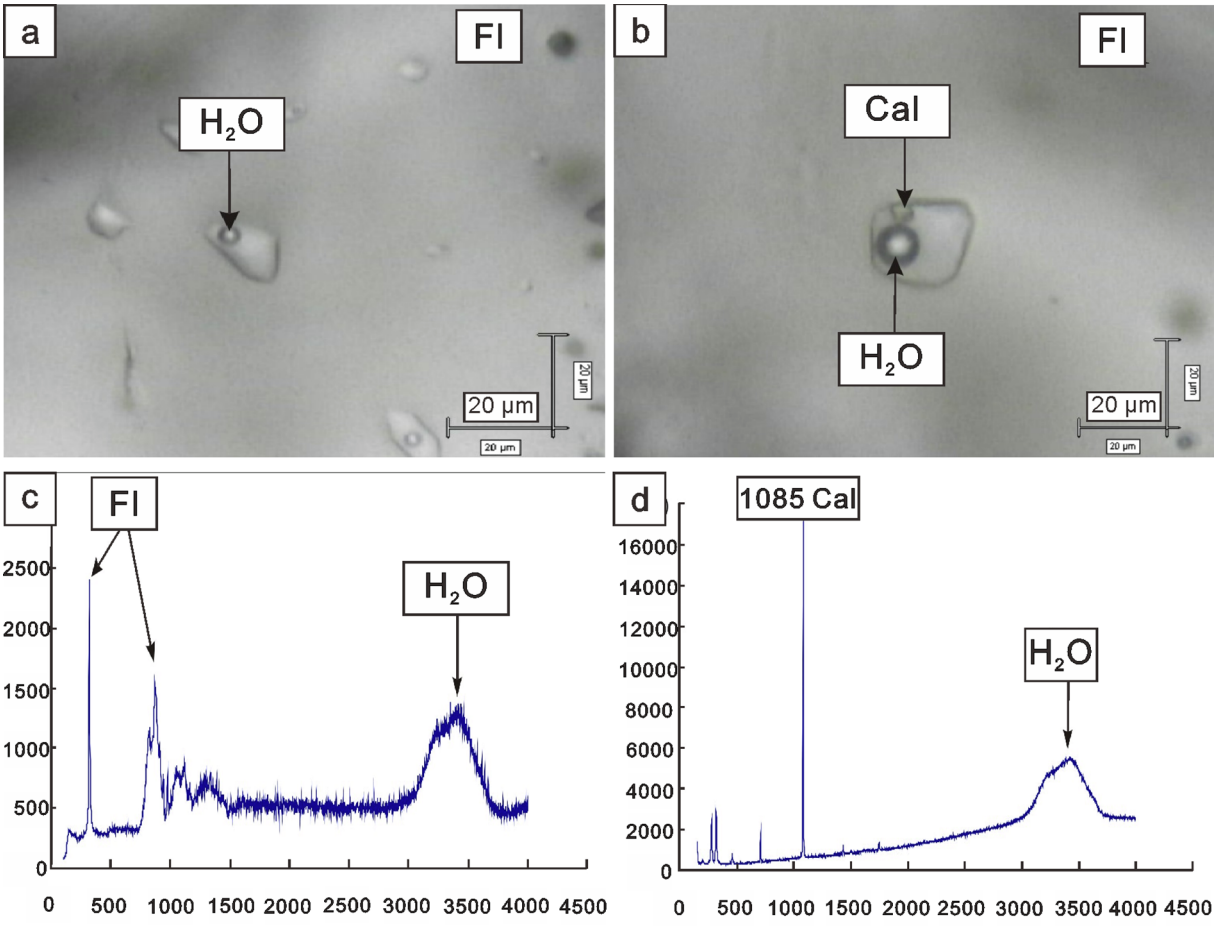

Fig. 6. Fluid inclusions microphotographs and Laser Raman spectra for fluid inclusions from the Dongzhongla Pb-Zn deposit. Fl, fluorite; Cal, calcite.

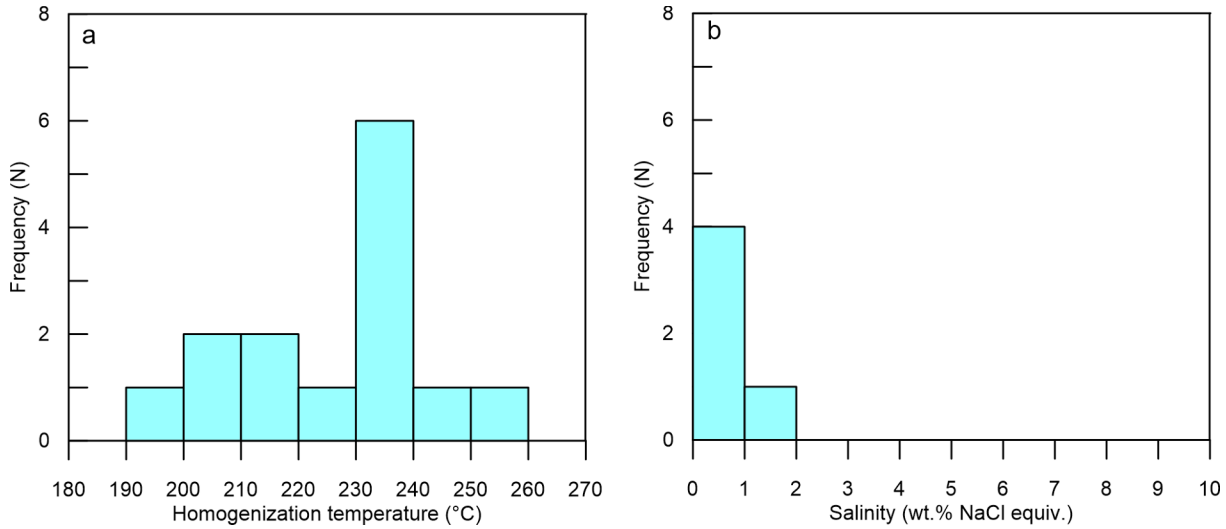

Fig. 7. Histograms of fluid inclusions homogenous temperature and salinity.

This indicates that the source of sulfur in ore-forming fluids has little relationship with sediment sulfur. In contrast, magmatic-derived sulfur has similar $\delta^{34}S$ values (0–5‰, Ohmoto, 1972) to those of sulfides, indicating a magmatic source of sulfur in the Dongzhongla deposit. Furthermore, compared with sulfur isotopic data of the nearby skarn Pb-Zn deposits that have clear contributions from basement-derived sulfur (Liu, 2008; Zhang et al., 2008; Wang, 2010; Wang et al., 2016; Fu et al., 2017), our sulfur isotopic data suggest that the sulfur in the Dongzhongla deposit is dominantly of magmatic origin.

6.1.2. Source of metals

Due to the extremely low concentrations of U and Th in galena, its radiogenic Pb isotopes are negligible (Carr et al., 1995; Pass et al., 2014; Zhou et al., 2015, 2016, 2018a; Luo et al., 2020). Hence, the Pb isotopic ratios of galena from the Dongzhongla deposit can reflect those of hydrothermal fluids.

It is clearly that the in situ Pb isotopic ratios show lineal trends in the diagrams of $^{207}Pb/^{204}Pb$ vs. $^{206}Pb/^{204}Pb$ and $^{208}Pb/^{204}Pb$ vs. $^{206}Pb/^{204}Pb$ (Fig. 14), which means: (1) simple mixing of two end-members (DePaolo and Wasserburg, 1979; Zheng and Hoefs, 1993), or (2) the gradually increasing radiogenic Pb isotopes during ore formation processes (Zhou et al., 2018c).

Mixing curves of two isotopically differentiated end-members usually form fusiform curves (DePaolo and Wasserburg, 1979; Zheng and Hoefs, 1993). Only when the contents derived from two end-members are the same (simple mixing model), would the mixing curve be a line. Actually, the mixing process may be too complex to produce lineal Pb isotopic variation, and the contributions of Pb from hydrothermal fluids and wall rocks are almost impossible to be the same. Otherwise, the variable C-H-O isotopic compositions of calcite and quartz from the Dongzhongla deposit (Fei et al., 2018) also suggest a sample mixing model may be impossible. Hence, the simple mixing model is unreasonable, and isochron may be the appropriate interpretation for lineal trends. Therefore, Pb was probably sourced from magmatic fluids, with negligible Pb from wall rocks.

Furthermore, the in situ Pb isotopic compositions of Gn1 are higher than those of Gn2 (Fig. 14), suggesting the initial U and Th contents of Gn1 are higher than those of Gn2. Moreover, Pb isotopic data in the diagram of $^{208}Pb/^{206}Pb$ vs. $^{207}Pb/^{206}Pb$ (Fig. 15) present three different linear trends, suggesting galena may have different Th/U ratios in different stages and different thin sections.

The in situ and bulk Pb isotopic ratios are plotted at the Pb evolution curve of the upper crust (Fig. 13) (Zartman and Doe, 1981), suggesting that the source of Pb is mainly from the upper crust. Previous study suggested that the Dongzhongla deposit was formed at ~42 Ma and was genetically linked with the Sharang Mo deposit that was formed at ~51 Ma (Fei et al., 2010a). However, Fig. 13 presents that Pb isotopic data of the Dongzhongla are different from those of the Sharang Mo deposit, which might have an influx of mantle materials and were consistent with the interpretation from Nd-Hf isotopic model of the Sharang intrusions (Zhao et al., 2016). The spatial distribution of skarn (Fig. 2a) shows directly genetic relationship between skarn and granite porphyry. Furthermore, the Pb isotopic ratios of galena are similar to those of the early Cretaceous intrusive rocks, indirectly confirming that the Pb-Zn mineralization was related to the early Cretaceous magmatic activities. The Pb isotopic ratios of the early Cretaceous intrusions are plotted at the Pb evolution curve of upper crust and are similar to those of the Lhasa basement, indicating they might be derived from partial melting from upper crust. This is consistent with negative zircon $\varepsilon_{Hf}(t)$ values (−19.7 to −10.6) reported by Gao et al. 2011a. Hence, we suggest Pb-rich Lhasa basement materials melted during early Cretaceous, resulting in the formation of S-Cl-Pb- and Zn-bearing felsic magma. The magma ascended and would have reached volatile saturation and released Pb-Zn-bearing aqueous fluids at shallow depth (1–2 km, Fei et al., 2010c; Hou et al., 2012), resulting in the skarn Pb-Zn mineralization.

6.2. Fluid evolution: Implications from the geochemistry of quartz crystals

Great variance in Al concentrations of single hydrothermal quartz crystal (Fig. 8c, d), where no evidence for a great temperature change, suggests that it do not caused by temperature fluctuations (Rusk et al., 2008). Previous studies suggested that Al concentrations of hydrothermal quartz may reflect the aqueous Al concentrations, which are dependent on pH values (Perny et al., 1992; Rusk et al., 2008). An increasing trend of the pH values would facilitate incorporation of Al^{4+} in the growing quartz crystal (Merino et al., 1989; Jourdan et al., 2009). Al concentrations of Qz1 mainly display two downward trends from core to rim (Fig. 8a, c), reflecting the gradually decreasing of pH values. The mechanism of pH values declining may be mixing with the acidic meteoric water (pH < 4), which was probably produced by the high atmospheric CO_2 levels (4–5 times higher than now) during the early Cretaceous (Berner, 1997; Berner and Kothavala, 2001). The H-O isotopic compositions ($\delta D = -127$ to −99‰ and $\delta^{18}O = -9.9$ to −4.0‰) of hydrothermal quartz also support the mixing model (Fei et al., 2010c). Therefore, the pH values of primary magmatic fluids may

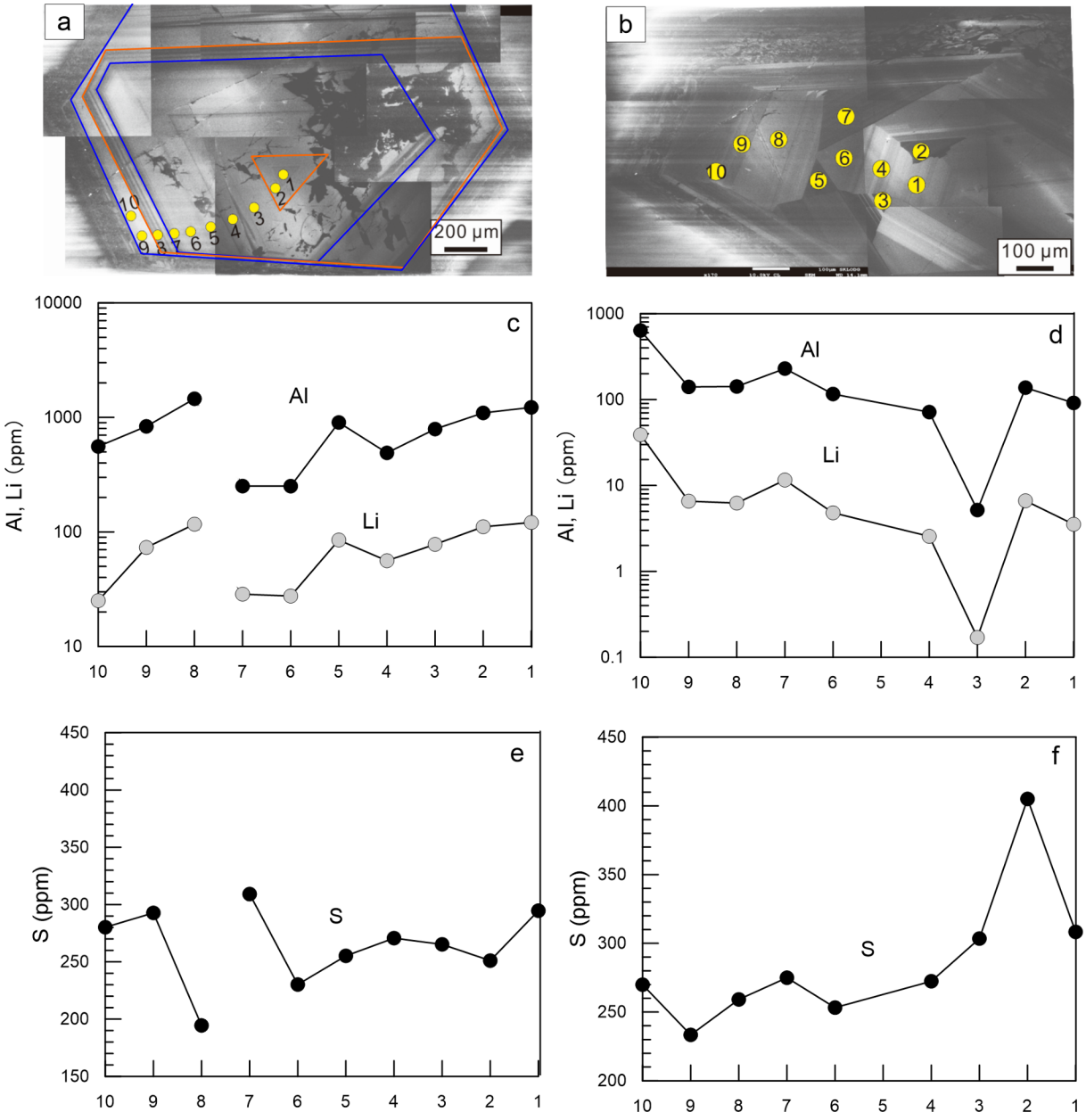

Fig. 8. Correlated CL image, LA-ICP-MS analyses of Qz1 (a) and Qz2 (b). Orange lines outlined the zones with high Al concentrations, while blue lines outlined the zones with low Al concentrations.

be higher than those of ore-forming fluids (5.3–5.5) calculated by Huo et al. (2012). Acidification of the magmatic fluids would increase solubility of complex and prevent the precipitation of sulfides. Moreover, the two Al-rich zones and the corresponding outer Al-poor zones (Fig. 8a, c) indicate periodic fluid influxes mixed with acidic meteoric water. In contrast, the increasing Al concentrations of Qz2 from core to rim may suggest neutralization of acidic ore-forming fluids, which may be caused by enhancement of W/R interaction (Zheng and Hoefs, 1993) and weakness of mixing with meteoric water.

It is clearly shown in Figs. 8c, d and 9a that Al and Li concentrations correlate in the hydrothermal quartz, which suggests Al^{3+} and Li^{+} form a coupled substitution for Si^{4+} in quartz lattice, presumably as $[AlO_4/Li^{+}]^0$ centers (Rusk et al., 2008, 2011; Jourdan et al., 2009). Furthermore, Li/Al ratios vary among samples or even vary among growth zones within single crystal. The Li/Al ratios of Qz2 (0.01–0.06, mean 0.04) are lower than those of Qz1 (0.05–0.14, mean 0.11), suggesting that other 1^{+}-cations should complete the charge, probably as $[AlO_4/(Li^{+}, Na^{+}, K^{+}, H^{+}]^0$ in Qz2. The Qz2 appears to have higher Na/Al ratios (Fig. 9c), but even Na is considered, the 1^{+}-cations/3^{+}-cations ratios of Qz2 are still lower than those of Qz1 (Fig. 9b). Therefore, H^{+} cations, which cannot be measured by using LA-ICPMS, likely account for the apparent 1^{+}-cations deficiency. Additionally, the Qz1 and Qz2 exhibit two different tendencies in the plot of Li/Al ratios vs. Al concentrations (Fig. 9e). Li/Al ratios of Qz2 increase logarithmically to high Al concentrations, suggesting that more Li^{+} correspond with AlO_4 during neutralization of acidic ore-forming fluids (H^{+} decrease). Li/Al ratios of Qz1 show a downward trend, indicating Li^{+} and Al^{+} have different behavior in acidification process (H^{+} increase).

Titanium (Ti) and Ge are the 4^{+}-cations that have concentrations mostly above the detection limits in hydrothermal quartz from the

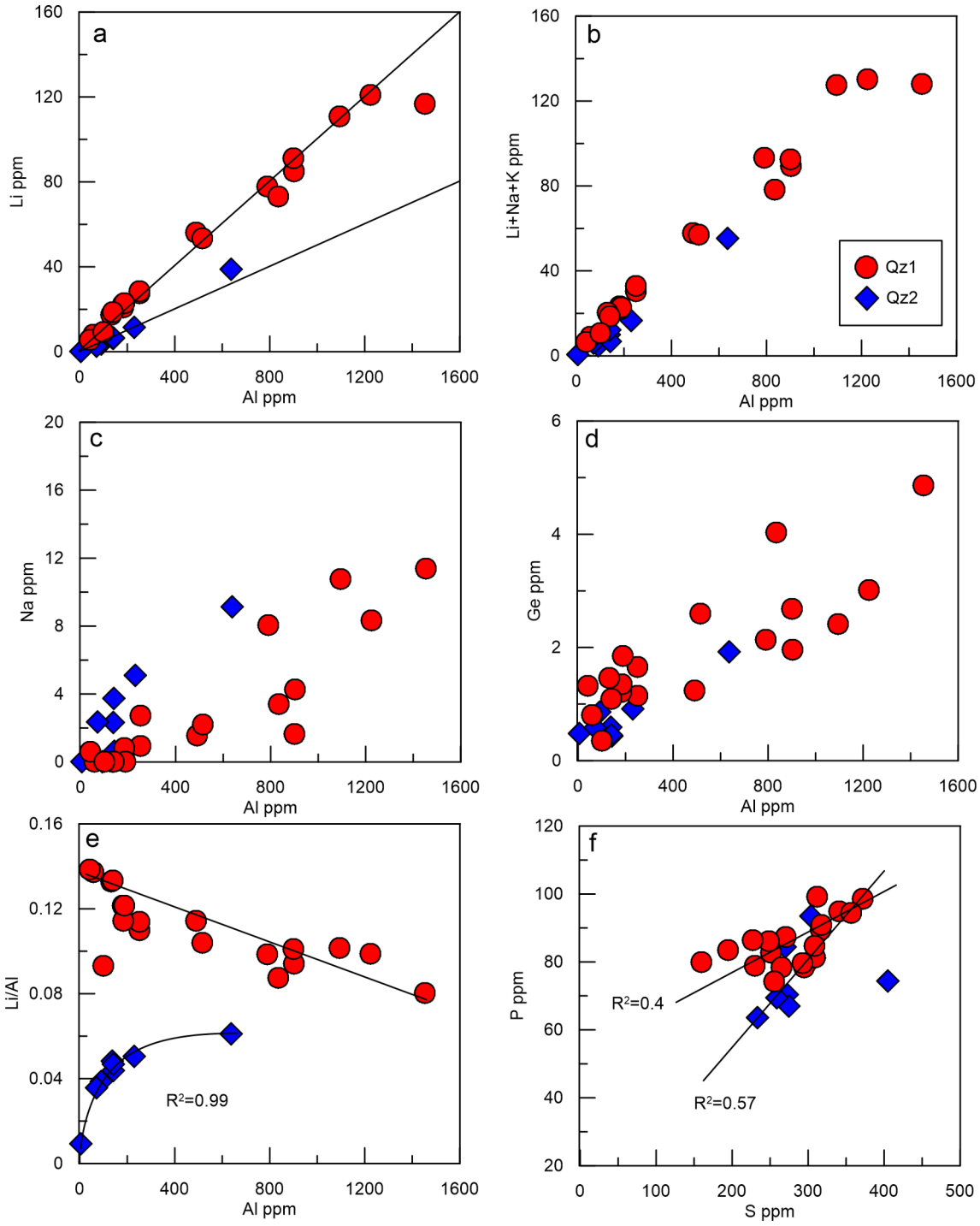

Fig. 9. Trace element correlation plots for hydrothermal quartz from the Dongzhongla Pb-Zn deposit.

Dongzhongla deposit. Incidentally, Ti does not have correlation with Ge. Ti^{4+} substitutes directly into the Si^{4+} site and does not correlate with 1^{+}-, 2^{+}- or 3^{+}- cations (Supplementary Table 2). Because Ti has an ionic radius that is larger than that of Si^{4+}, it prefers to replace Si^{4+} in quartz at high temperatures (Jourdan et al., 2009). Hence, this substitution is used as a geothermometer applied in igneous rocks or hydrothermal systems (Wark and Watson, 2006; Huang and Audétat, 2012). We estimated the formation temperatures of hydrothermal quartz are 336–427 °C (mean 373 °C) of Qz1 and 358–461 °C (mean 386 °C) of Qz2 by TitaniQ thermometer (Wark and Watson, 2006). The estimated temperatures of Qz2 are close to, but slightly higher than those of Qz1, indirectly suggesting the weakness of mixing with low temperature meteoric water.

Ge^{4+} has a similar ionic radius and the same charge as Si^{4+}. The present results show a general correlation between Ge and Al (Fig. 9d), which was also reported in quartz from the Alpine veins by Jourdan et al. (2009). This correlation may suggest more substitutions of Ge^{4+} for Si^{4+} when more $[AlO_4/Li]$ forms.

Calcium (Ca) may be mainly concentrated in fluid inclusions or mineral inclusions in quartz (Götze, 2009; Götze et al., 2001; Lan et al., 2017). The Ca concentrations are higher than detection limit only in few spot analyses (87–594 ppm), suggesting occurrence of calcite

Table 1
C-O isotopic compositions of calcite and limestone from the Dongzhongla Pb-Zn deposit.

Sample No.	Mineral/Rock	$\delta^{13}C_{PDB}$ (‰)	$\delta^{18}O_{PDB}$ (‰)	$\delta^{18}O_{SMOW}$ (‰)
DZL-3	Calcite	−3.6	−27.9	2.1
DZL-4	Calcite	−3.7	−27.7	2.3
DZL-8	Calcite	0.3	−25.4	4.7
DZL-13	Calcite	−1.0	−26.4	3.6
DZL-18	Calcite	−5.1	−28.2	1.7
DZL-21	Calcite	−4.1	−28.0	2.0
DZL-29	Calcite	−0.2	−27.4	2.6
DZL-37	Fresh Limestone	2.3	−10.7	19.8
DZL-10	Altered Limestone	−1.5	−16.8	13.5
DZL-19	Altered Limestone	−2.4	−22.1	8.0
DZL-23	Altered Limestone	2.3	−15.0	15.4
DZL-39	Altered Limestone	3.8	−14.7	15.7

micro-inclusions or fluid inclusions. One spot analysis of Qz1 (DZL-29-1-10) exhibits correlation between Ca and other cations (Na^+, K^+ and Fe^{2+}), indicating that fluid inclusions may be in the scale of this laser spot. This spot analysis has high iron concentration (302 ppm), suggesting ore-forming fluids were Fe-rich during early phase. One spot analysis of Qz2 (DZL-29-2-6) shows abnormally high Ca (594 ppm), Na (41.7 ppm), K (7.5 ppm), Cu (39.7 ppm), and Zn (3.87 ppm) concentrations, reflecting ore-forming fluids contain high Ca, Cu and Zn concentrations during the late phase. The extremely high Ca concentrations of the late phase fluids may be sourced from limestone, which reacted with acidic ore-forming fluids.

The occurrence of sulfur in quartz from the Dongzhongla deposit, which is seldom reported in the literature, is important to address. Sulfur concentrations of hydrothermal quartz are high and do not correspond with occurrence of fluid inclusions and micro-inclusions, suggesting that sulfur may be in crystal structure of quartz. Fig. 9f shows that sulfur concentrations are correlated with P concentrations, suggesting charge-pairing between $[PO_4]^+$ and S^{2-} may be possible, although S^{2-} has a large ionic radius. Fig. 9f also shows that S and P concentrations of Qz1 and Qz2 have different linear trends, reflecting physical-chemical condition difference between early and late phase fluids. Since temperature does not show an obvious fluctuation, pH values may account for this difference.

Furthermore, the sulfur concentrations of hydrothermal quartz are similar with those of fluid inclusions (Supplementary Table 2), indicating they can reflect those of ore-forming fluids. Sulfur

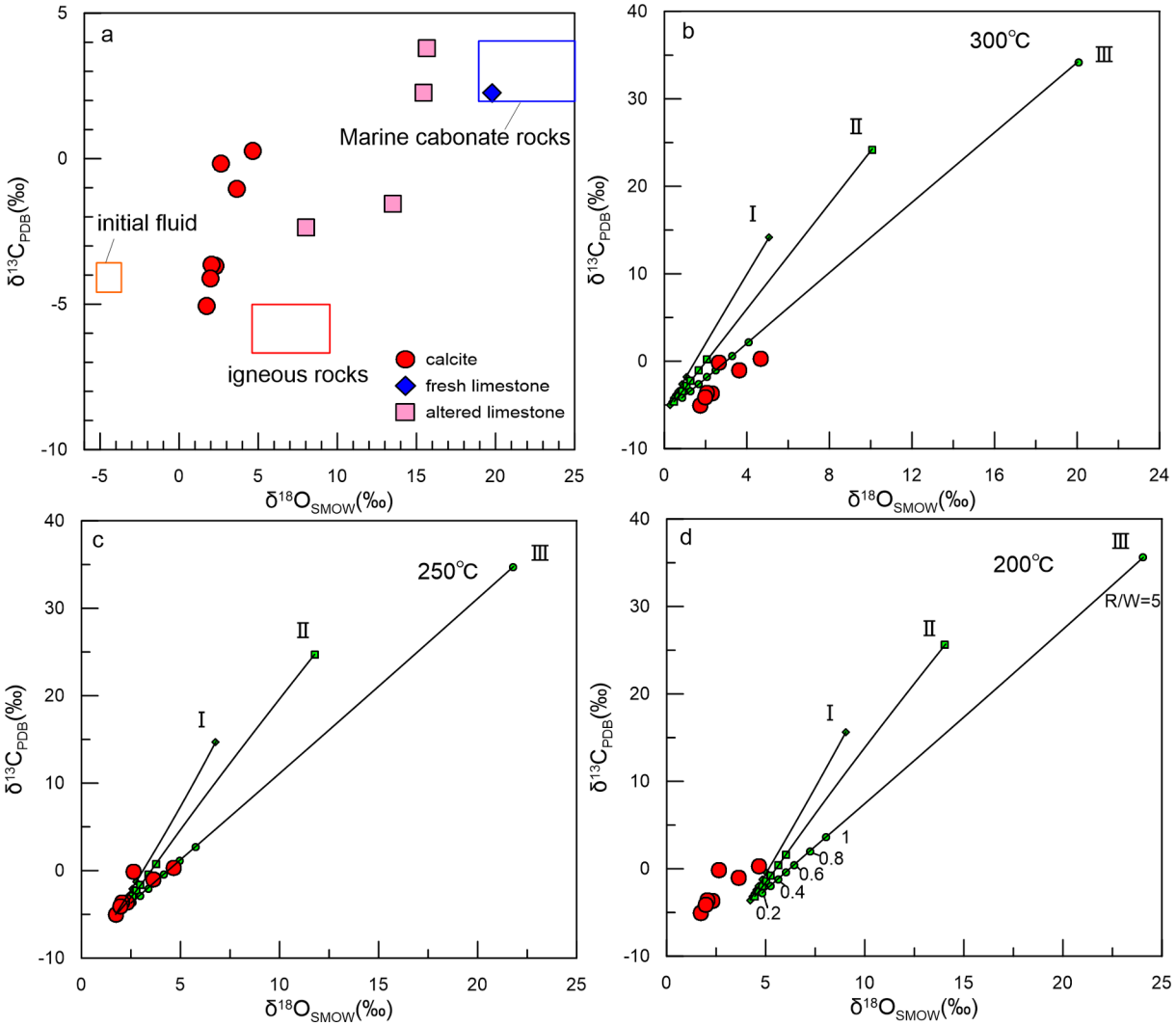

Fig. 10. Carbon vs. oxygen isotopic variations of hydrothermal calcite from the Dongzhongla Pb-Zn deposit. Initial fluids: $\delta^{13}C$ = -4‰; $\delta^{18}O$ = -5‰. I: $\Delta^{13}C$ = 4‰, $\Delta^{18}O$ = 1‰; II: $\Delta^{13}C$ = 6‰, $\Delta^{18}O$ = 2‰; III: $\Delta^{13}C$ = 8‰, $\Delta^{18}O$ = 4‰.

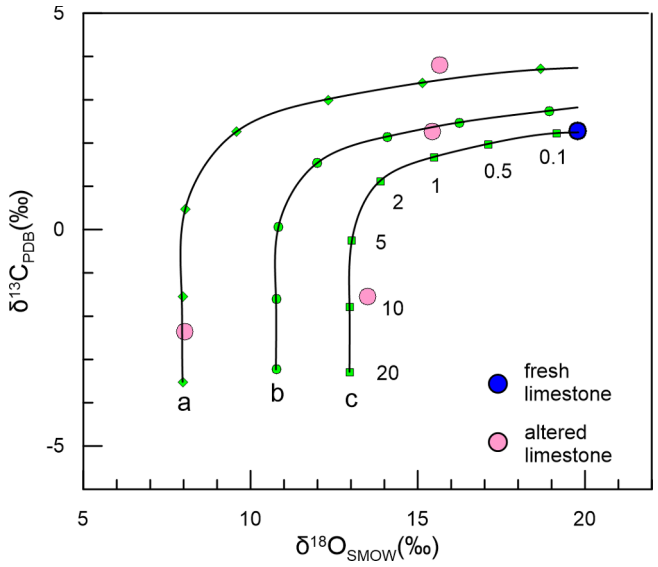

Fig. 11. Carbon vs. oxygen isotopic compositions of limestone from the Dongzhongla Pb-Zn deposit. C-O isotopic compositions of fluids: a. $\delta^{13}C$ = -3.5‰; $\delta^{18}O$ = 1.2‰; b. $\delta^{13}C$ = -3.0‰; $\delta^{18}O$ = 4.0‰ and c. $\delta^{13}C$ = -3.0‰; $\delta^{18}O$ = 6.2‰.

Table 2
S isotopic compositions of sulfides from the Dongzhongla Pb-Zn deposit.

Sample No.	Minerals	$\delta^{34}S_{CDT}$ (‰)	SE
DZL-5-1	Galena	2.13	0.04
DZL-29	Galena	2.51	0.01
DZL-25	Galena	2.71	0.08
DZL-27	Galena	2.85	0.06
DZL-36	Galena	2.89	0.05
DZL-22	Galena	2.79	0.08
DZL-26	Galena	2.42	0.07
DZL-28	Sphalerite	3.99	0.14
DZL-18	Pyrite	3.53	0.06

concentrations of Qz1 (200–280 ppm) are consistent. In contrast, sulfur contents of Qz2 decline from 410 to 230 ppm with growth zones (Fig. 8f), indicating the sulfur contents in late phase fluids decreased gradually. The decrease of sulfur concentrations is related to precipitation of sulfides. Several processes can result in the precipitation of sulfides, such as cooling, phase separation and pH change. The estimated temperatures of Qz2 are slightly higher than those of Qz1, suggesting temperature cannot account for sulfides formation. Furthermore, fluid inclusion studies exclude the possibility of phase separation during quartz-sulfide stage (Fei et al., 2010c). Finally, the negative correlation between S and Al in Qz2 (Fig. 8f) may suggest sulfide precipitation process (sulfur decrease) was caused by neutralization of acidic fluids (Al increase).

6.3. Water/rock interaction during the fluorite-calcite-sulfide stage

Fluid inclusions in fluorite show that ore-forming fluids in fluorite-calcite-sulfide stage have low temperatures and salinities. Furthermore, the minimum trapping temperature can be estimated by the T_{hTOT} (200–250 ˚C) (Diamond, 2001). Otherwise, calcite crystals in fluid inclusions within fluorite suggest that W/R interaction increased the Ca concentrations in ore-forming fluids, and caused fluorite and calcite precipitation simultaneously. Hence, the formation temperatures of fluorite can be used for calcite. Therefore, the largest estimated trapping temperature (250 ˚C) was used to calculate the C-O isotopic compositions of hydrothermal fluids and W/R interaction processes as follows.

The C-O isotopic compositions of hydrothermal calcite show trend toward limestone (Fig. 10a), indicating calcite precipitated in the case of W/R interaction, when H_2CO_3 acts as the dominant dissolved carbon species (Zheng and Hoefs, 1993). Therefore, $\delta^{13}C_{H2CO3}$ values can represent the $\delta^{13}C_{fluid}$ values. Additionally, H_2CO_3 isotopically behaves like CO_2, so that the fractionation involving CO_2 is applied when H_2CO_3 is involved (Zheng and Hoefs, 1993). Based on the trapping temperature (250 ˚C), the $\delta^{13}C_{H2CO3}$ and $\delta^{18}O_{H2O}$ values of initial fluids are −4‰ and −5‰, respectively, calculated by functions of $1000\ln\alpha_{(calcite\text{-}CO2)} = 2.988 \times 10^6/T^2 - 7.663 \times 10^3/T + 2.4612$ (Bottinga, 1968) and $1000\ln\alpha_{(calcite\text{-}H2O)} = 2.78 \times 10^6/T^2 - 3.39$ (O'Neil et al., 1969). The initial $\delta^{13}C_{fluid}$ value is similar to those of

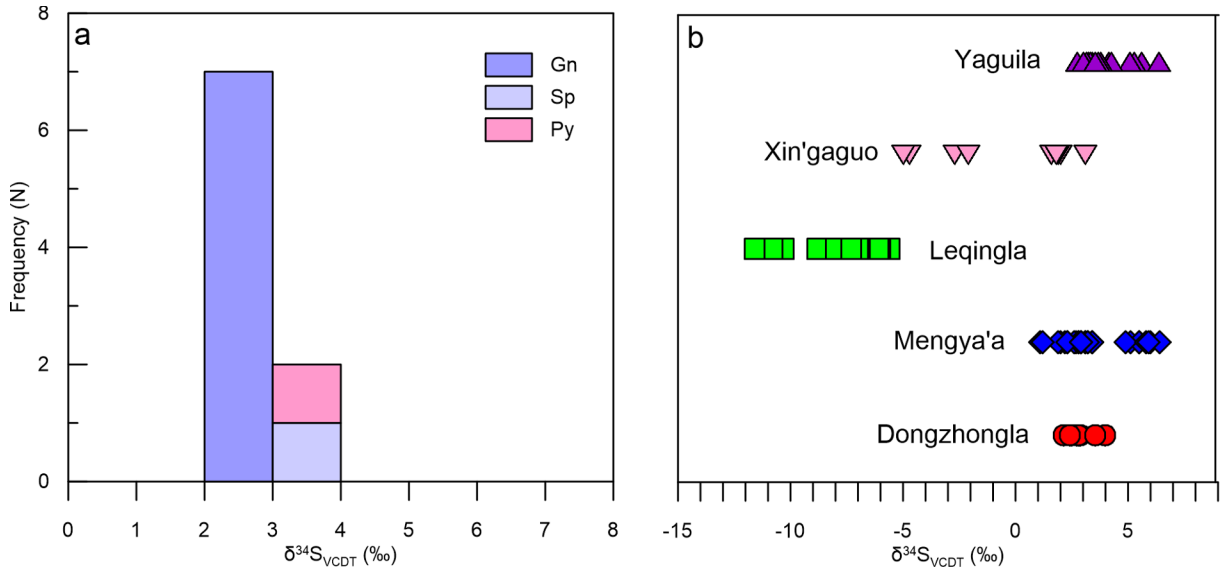

Fig. 12. Histograms of sulfur isotopic data for sulfides from the Dongzhongla (a) and the nearby skarn Pb-Zn deposits (b). Sulfur isotopic data for the nearby skarn Pb-Zn deposits are taken from Fu et al. (2017), Liu (2008), Zhang et al. (2008), Wang (2010) and Wang et al. (2016).

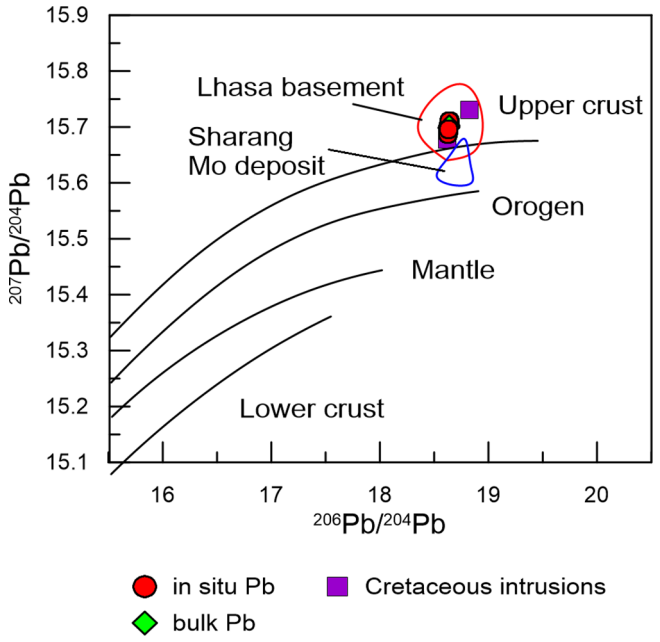

Fig. 13. Pb isotopic ratios of galena from the Dongzhongla Pb-Zn deposit (modified after Zartman and Doe, 1981). Pb isotopic data of the Lhasa basement and Sharang Mo deposit are sourced from Gariépy et al. (1985) and Sun et al. (2017), respectively.

igneous rocks (Taylor et al., 1967), suggesting the C is mainly from magmatic sources. However, the calculated initial $\delta^{18}O_{fluid}$ value is lower than those of magmatic (+5.5 to +10‰, Taylor, 1974) and metamorphic water (+5 to +25‰, Taylor, 1974), but is similar to some of the mixed water (−10 to −5‰) in the Dongzhongla deposit (Fei et al., 2018), indicating the O is from a mixed source of ^{18}O-depleted meteoric water and ^{18}O-enriched magmatic water.

As discussed above, the hydrothermal calcite was deposited from ore-forming fluids due to W/R interaction. Hence, the C-O isotopic compositions of hydrothermal calcite can be used to estimate the forming temperatures, rock/water (R/W) ratios and changes in C-O isotopic compositions of wall rocks (Zheng and Hoefs, 1993; Pili et al., 2002; Du et al., 2017; Zhou et al., 2018a,b). Assuming that R/W ratios range from 0.2 to 5, and temperatures are 300 °C, 250 °C and 200 °C, we calculated the theoretical curves for H_2CO_3 as the dominant dissolved carbon species, as shown in Fig. 10. The initial fluids have $\delta^{13}C$ and $\delta^{18}O$ values of −4‰ and −5‰, respectively. Fig. 10 illustrates that hydrothermal calcite mainly precipitated at temperatures of 250–300 °C, with R/W ratios ranging of 0.2–1, and the changes in the $\delta^{13}C$ and $\delta^{18}O$ values of wall rocks were up to 4‰ and 8‰, respectively.

The $\delta^{13}C$ and $\delta^{18}O$ values of altered limestone can reflect the $\delta^{13}C$ and $\delta^{18}O$ values of ore-forming fluids and W/R ratios (Vazquez et al., 1998; Large et al., 2001). A set of isotopic mixing curves is presented in Fig. 11 for exchange of limestone with hydrothermal fluids at 250 °C having H_2CO_3 values of 0.1. $\delta^{13}C$ = 2.8–3.8‰ and $\delta^{18}O$ = 19.8‰ are considered to represent the isotopic compositions of fresh limestone rocks. Fig. 11 shows that the altered limestone rocks with variable $\delta^{13}C$ and $\delta^{18}O$ values were caused by interaction with ore-forming fluids that have different isotopic compositions, indicating the isotopic compositions of these fluids changed during W/R interaction. In addition, the altered limestone rocks with lower $\delta^{18}O$ values have low W/R ratios (0.5–1) (Fig. 11), while those with lower $\delta^{13}C$ and $\delta^{18}O$ values have high W/R ratios (~10) (Fig. 11), suggesting intense W/R interaction not only changed isotopic compositions but increased porosity of wall rocks.

6.4. Implications for ore formation processes

The ore formation processes of the Dongzhongla skarn Pb-Zn deposit were illustrated in Fig. 16. The geochronological and geochemical evidence of granite porphyries suggest that the tectonic setting of the studied region was related to the slab rollback of the subducted Bangong-Nujiang Oceanic slab during early Cretaceous (e.g. Zhu et al., 2009, 2011). This rollback would lead to the asthenospheric upwelling (Royden, 1993; Zheng and Dai, 2018; Wu et al., 2019), which induced crustal melting (Sun et al., 2019), and then generated felsic magma. The magma migrated upward, intruded into the Luobadui Formation strata, and began to cool and crystalize. During the cooling and degassing processes, sulfur- and metal-rich fluids were released from the magma and then interacted with the Luobadui Formation limestone. Skarn minerals (such as diopside and actinolite) formed first (Fig. 16a) and then the fractures formed in skarn and wall rocks. These fractures led to

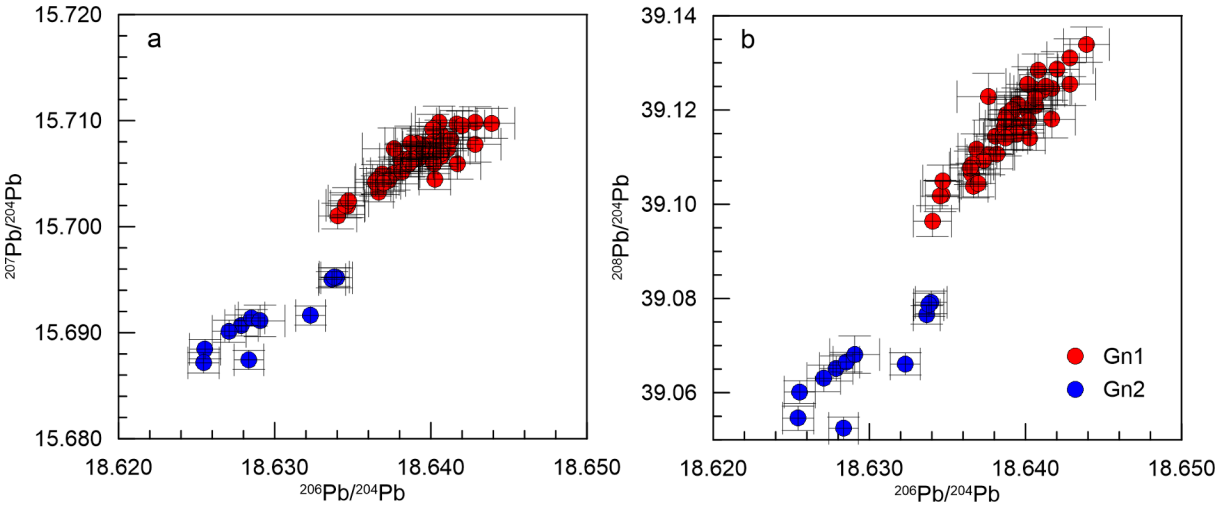

Fig. 14. Plots of $^{207}Pb/^{204}Pb$ vs. $^{206}Pb/^{204}Pb$ (a) and $^{208}Pb/^{204}Pb$ vs. $^{206}Pb/^{204}Pb$ (b).

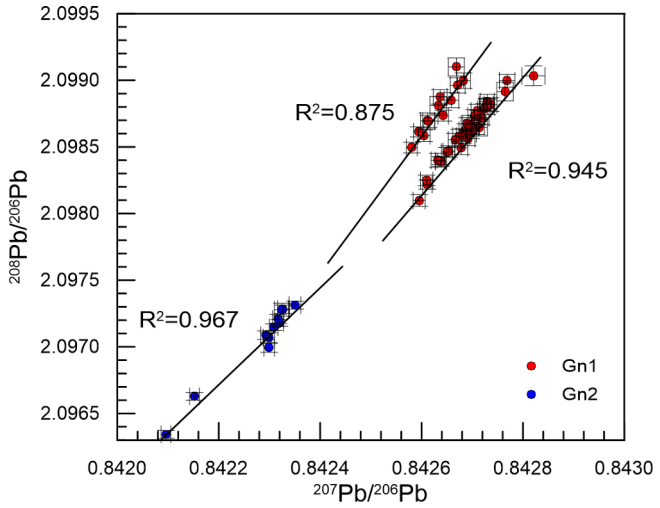

Fig. 15. Plot of $^{208}Pb/^{206}Pb$ vs. $^{207}Pb/^{206}Pb$.

the mixing of magmatic fluids and meteoric water, causing the precipitation of Qz1 at 336–427 °C (mean 373 °C). The addition of acidic meteoric water resulted in a decrease in pH values, which restrained the precipitation of sulfides in the early phase (Fig. 16b). With the decrease of the portion of mixing, the W/R interaction played an important role in neutralizing the acidic ore-forming fluids during the late phase and caused the formation of Qz2-sulfide veins at 358–461 °C (mean 386 °C) (Fig. 16b). The continuous W/R interaction caused the increasing concentrations of Ca^{2+} and decreasing concentrations of H^{+} in ore-forming fluids (Fig. 16c) (Ohmoto, 1972). Essentially, the increase in pH values caused the precipitation of fluorite-calcite-sulfide veins at 250–300 °C.

7. Conclusions

(1) The sources of ore-forming elements for the Dongzhongla skarn Pb-Zn deposit are associated with the early Cretaceous felsic magmatism.
(2) The decreasing Al and consistent sulfur concentrations in Qz1 indicate that the acidification process may restrain the precipitation of sulfides during the early phase. The increasing Al and decreasing sulfur concentrations in Qz2 suggest that the precipitation of sulfides was caused by neutralization process during the late phase.
(3) Fluorite-calcite-sulfide veins were formed at the temperatures of 250–300 °C. The W/R interaction led to the precipitation of calcite, and the variations in C-O isotopes of the calcite and altered limestone rocks.

CRediT authorship contribution statement

Guotao Sun: Conceptualization, Formal analysis, Visualization, Writing - original draft. **Jia-Xi Zhou:** Supervision, Project administration, Funding acquisition. **Kai Luo:** Investigation. **Zhen-Zhong Xiang:** Investigation. **Zhi-An Bao:** Methodology. **Tao Sun:** Writing - review & editing.

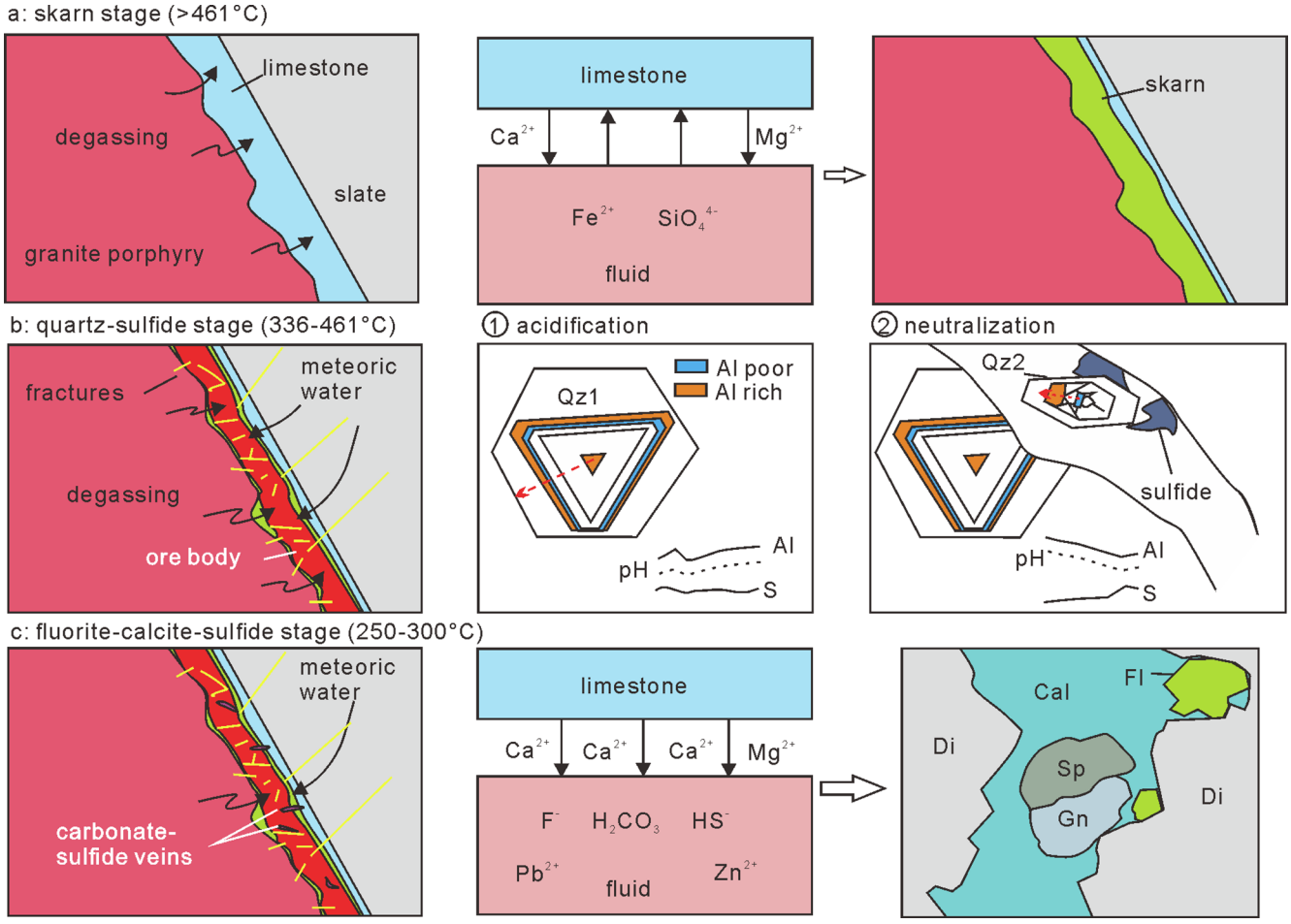

Fig. 16. Schematic model for ore formation processes of the Dongzhongla Pb-Zn deposit. (a) Skarn stage, (b) quartz-sulfide stage, and (c) fluorite-calcite-sulfide stage.

Declaration of Competing Interest

The authors declare that they have no known competing financial interests or personal relationships that could have appeared to influence the work reported in this paper.

Acknowledgments

This study was financially supported by the National Natural Science Foundation of China (41872095, U1812402 and 41430315), the National Key R&D Project of China (2017YFC0602502), Yunnan Applied Basic Research Project (2018FB079) and the Research Startup Project (YJRC4201804) and the Cultivation Project (2018YDJQ009) of Yunnan University to J.-X. Zhou. We would like to thank the researchers in the laboratories of fluid inclusions, SEM, LA-ICPMS, and stable isotopes at the Institute of Geochemistry, Chinese Academy of Sciences for their analytical works. Comments and suggestions from Prof. Mei-Fu Zhou (Editor-in-Chief), and three anonymous reviewers significantly improved the quality of this paper.

Appendix A. Supplementary material

Supplementary data to this article can be found online at https://doi.org/10.1016/j.jseaes.2019.104215.

References

Allan, M.M., Yardley, B.W.D., 2007. Tracking meteoric infiltration into a magmatic-hydrothermal system: A cathodoluminescence, oxygen isotope and trace element study of quartz from Mt. Leyshon, Australia. Chem. Geol. 240, 343–360.

Allégre, C.J., Courtillot, V., Tapponnier, P., Hirn, A., Mattauer, M., Coulon, C., Jaeger, J.J., Achache, J., Schärer, U., Marcoux, J., Burg, J.P., Girardeau, J., Armijo, R., Gariépy, C., Göpel, C., Tindong, L., Xuchang, X., Chenfa, C., Guangqin, L., Baoyu, L., Jiwen, T., Naiwen, W., Guoming, C., Tonglin, H., Xibin, W., Wanming, D., Huaibin, S., Yougong, C., Ji, Z., Hongrong, Q., Peisheng, B., Songchan, W., Bixiang, W., Yaoxiu, Z., Xu, R., 1984. Structure and evolution of the Himalaya-Tibet orogenic belt. Nature 307, 17–22.

Audétat, A., Garbe-Schönberg, D., Kronz, A., Pettke, T., Rusk, B., Donovan, J.J., Lowers, H.A., 2015. Characterisation of a natural quartz crystal as a reference material for microanalytical determination of Ti, Al, Li, Fe, Mn, Ga and Ge. Geostand. Geoanal. Res. 39, 171–184.

Bao, Z.A., Yuan, W.T., Yuan, H.L., Liu, X., Chen, K.Y., Zong, C.L., 2016. Non-matrix-matched determination of lead isotope ratios in ancient bronze artifacts by femtosecond laser ablation multi-collector inductively coupled plasma mass spectrometry. Int. J. Mass Spectrom. 402, 12–19.

Berner, R.A., 1997. The rise of plants and their effect on weathering and atmospheric CO_2. Science 276, 544–546.

Berner, R.A., Kothavala, Z., 2001. Geocarb III: a revised model of atmospheric CO_2 over phanerozoic time. Am. J. Sci. 301, 182–204.

Blisniuk, P.M., Hacker, B.R., Glodny, J., Ratschbacher, L., Bi, S., Wu, Z., McWilliams, M.O., Calvert, A., 2001. Normal faulting in central Tibet since at least 13.5 Myr ago. Nature 412, 628–632.

Bottinga, Y., 1968. Calculation of fractionation factors for carbon and oxygen isotopic exchange in the system calcite-carbon dioxide-water. J. Phys. Chem. 72, 800–808.

Carr, G.R., Dean, J.A., Suppel, D.W., Heithersay, P.S., 1995. Precise lead isotope fingerprinting of hydrothermal activity associated with Ordovician to Carboniferous metallogenic events in the Lachlan fold belt of New South Wales. Econ. Geol. 90, 1467–1505.

Chu, M.F., Chung, S.-L., Song, B., Liu, D., O'Reilly, S.Y., Pearson, N.J., Ji, J., Wen, D.-J., 2006. Zircon U-Pb and Hf isotope constraints on the Mesozoic tectonics and crustal evolution of southern Tibet. Geology 34, 745–748.

Coleman, M., Hodges, K., 1995. Evidence for Tibetan plateau uplift before 14 Myr ago from a new minimum age for east–west extension. Nature 374, 49–52.

Collerson, K.D., Kamber, B.S., Schoenberg, R., 2002. Applications of accurate, high-precision Pb isotope ratio measurement by multi-collector ICP-MS. Chem. Geol. 188, 65–83.

Cui, X.L., Tang, J.X., Dorji, Zhong, K.H., Gao, Y.M., Liu, H.F., Zhang, J.S., Wang, C.H., Liu, T.T., 2011. Zircon U-Pb age of the quartz porphyry from Dongzhongla Pb-Zn deposit in Tibet, China. J. Chengdu Univ. Technol. (Sci. Technol.) 38, 557–562 (in Chinese with English abstract).

DePaolo, D.J., Wasserburg, G.J., 1979. Petrogenetic mixing models and Nd-Sr isotopic patterns. Geochim. Cosmochim. Acta 43, 615–627.

Diamond, L.W., 2001. Review of the systematics of CO_2–H_2O fluid inclusions. Lithos 55, 69–99.

Du, L.J., Li, B., Huang, Z.L., Zhou, J.X., Zou, G.F., Yan, Z.F., 2017. Carbon-oxygen isotopic geochemistry of the Yangla Cu skarn deposit, SW China: Implications for the source and evolution of hydrothermal fluids. Ore Geol. Rev. 88, 809–821.

Einaudi, M., Meinert, L.D., Newberry, R., 1981. Skarn deposits. Econ. Geol. 75, 317–391.

Fei, G.C., Wen, C.Q., Wang, C.S., Zhou, X., Wu, P.Y., Wen, Q., 2010a. Laser microprobe ^{40}Ar-^{39}Ar geochronology of quartz from Dongzhongla lead-zinc deposit in Tibet and its significance. J. Miner. Petrol. 30, 38–43 (in Chinese with English abstract).

Fei, G.C., Wen, C.Q., Wang, C.S., Zhou, X., Wu, P.Y., Wen, Q., Zhou, Y., 2010b. Zircon SHRIMP U-Pb age of porphyry granite in the Dongzhongla lead-zinc deposit, Maizhokunggar County, Tibet. Geol. China 37, 470–476 (in Chinese with English abstract).

Fei, G.C., Wen, C.Q., Zhou, X., Wu, P.Y., Hu, Y., Li, B.H., Long, X.L., 2010c. Research of mineralization fluids in the Dongzhongla lead-zinc deposit. Tibet. Geol. Explor. 46, 576–582 (in Chinese with English abstract).

Fei, G.C., Wen, C.Q., Wang, C.S., Wu, P.Y., Wen, Q., Zhou, X., 2010d. Zircon SHRIMP U-Pb and its geological significance in Dongzhongla allgovite, Mozhugongka area, eastern segment if Gangdese, Tibet, China. Geol. Bull. China. 29, 1138–1142 (in Chinese with English abstract).

Fei, G.C., Zhou, Y., Deng, Y., Chen, X., Wen, C.Q., Yu, Q., Ding, F., Zhou, X., Huo, Y., 2018. Geology and isotope geochemistry of the Dongzhongla Pb–Zn deposit in Tibet: implications for the origin of the ore-forming fluids and storage condition of certain metals. Resour. Geol. 68, 227–243.

Friedman, I., O'Neil, J.R., 1977. Compilation of stable isotope fractionation factors of geochemical interest. Data of Geochemistry. U.S. Geol. Surv. Prof. Pap. 1–12 (440–KK).

Fu, Q., Xu, B., Zheng, Y.C., Yang, Z.S., Hou, Z.Q., Huang, K.X., Liu, Y.C., Zhang, C., Zhao, L., 2017. Two episodes of mineralization in the Mengya'a deposit and implications for the evolution and intensity of Pb–Zn–(Ag) mineralization in the Lhasa terrane, Tibet. Ore Geol. Rev. 90, 877–896.

Galer, S.J.G., Abouchami, W., 1998. Practical application of lead triple spiking for correction of instrumental mass discrimination. Mineral. Mag. A 62, 491–492.

Gao, Y.M., Chen, Y.C., Wang, C.H., Hou, K.J., 2011a. Zircon Hf isotopic characteristics and constraints on petrogenesis of Mesozoic-Cenozoic magmatic rocks in Nyainqentanglha region, Tibet. Miner. Depos. 30, 279–291 (in Chinese with English abstract).

Gao, Y.M., Chen, Y.C., Tang, J.X., Li, C., Li, X.F., Gao, M., Cai, Z.C., 2011b. Re–Os dating of molybdenite from the Yaguila porphyry molybdenum deposit in Gongbo'gyamda area, Tibet, and its geological significance. Geol. Bull. China 30, 1027–1036 (in Chinese with English abstract).

Gao, Y.M., Lan, Z.W., Chen, Y.C., Tang, J.X., 2017. Geochronological and geochemical constraints on the origin of Yaguila Cretaceous and Palaeogene ore-bearing quartz porphyries, Central Lhasa Terrane. Tibet. Geol. J. 52, 45–66.

Gariépy, C., Allègre, C.J., Xu, R.H., 1985. The Pb-isotope geochemistry of granitoids from the Himalaya-Tibet collision zone: implications for crustal evolution. Earth Planet. Sci. Lett. 74, 220–234.

Gaspar, M., Knaack, C., Meinert, L.D., Moretti, R., 2008. REE in skarn systems: a LA-ICP-MS study of garnets from the Crown Jewel gold deposit. Geochim. Cosmochim. Ac. 72, 185–205.

Götze, J., 2009. Chemistry, textures and physical properties of quartz – geological interpretation and technical application. Mineral. Mag. 73, 645–671.

Götze, J., Plötze, M., Habermann, D., 2001. Origin, spectral characteristics and practical applications of the cathodoluminescence (CL) of quartz – a review. Miner. Petrol. 71, 225–250.

Harlov, D.E., Austrheim, H., 2013. Metasomatism and the chemical transformation of rock: rock-mineral-fluid interaction in terrestrial and extraterrestrial environments. In: Harlov, D.E., Austrheim, H. (Eds.), Metasomatism and the Chemical Transformation of Rock: The Role of Fluids in Terrestrial and Extraterrestrial Processes, Lecture Notes in Earth System Sciences. Springer Berlin Heidelberg, Berlin, Heidelberg, pp. 1–16.

Hou, Z.Q., Yang, Z.M., Qu, X.M., Meng, X.J., Li, Z.Q., Beaudoin, G., Rui, Z.Y., Gao, Y.F., Zaw, K., 2009. The Miocene Gangdese porphyry copper belt generated during post-collisional extension in the Tibetan Orogen. Ore Geol. Rev. 36, 25–51.

Hou, Z.Q., Gao, Y.F., Qu, X.M., Rui, Z.Y., Mo, X.X., 2004. Origin of adakitic intrusives generated during mid-Miocene east–west extension in southern Tibet. Earth Planet. Sci. Lett. 220, 139–155.

Hou, Z.Q., Zheng, Y.C., Zeng, L.S., Gao, L.E., Huang, K.X., Li, W., Li, Q.Y., Fu, Q., Liang, W., Sun, Q.Z., 2012. Eocene-Oligocene granitoids in southern Tibet: Constraints on crustal anatexis and tectonic evolution of the Himalayan orogen. Earth Planet. Sci. Lett. 349–350, 38–52.

Huang, R.F., Audétat, A., 2012. The titanium-in-quartz (TitaniQ) thermobarometer: a critical examination and re-calibration. Geochim. Cosmochim. Acta 84, 75–89.

Huang, X.W., Gao, J.F., Qi, L., Meng, Y.M., Wang, Y.C., Dai, Z.H., 2016. In-situ LA–ICP–MS trace elements analysis of magnetite: The Fenghuangshan Cu–Fe–Au deposit, Tongling, Eastern China. Ore Geol. Rev. 72, 746–759.

Huo, Y., Wen, C.Q., Chen, H.D., Fei, G.C., 2012. The fluid inclusion physicochemical characteristics of Dongzhongla lead-zinc deposit. Met. Min. 435, 93–98 (in Chinese with English abstract).

Ji, W.Q., Wu, F.Y., Chung, S.L., Li, J.X., Liu, C.Z., 2009. Zircon U-Pb geochronology and Hf isotopic constraints on petrogenesis of the Gangdese batholith, southern Tibet. Chem. Geol. 262, 229–245.

Jourdan, A.L., Vennemann, T.W., Mullis, J., Ramseyer, K., Spiers, C.J., 2009. Evidence of growth and sector zoning in hydrothermal quartz from Alpine veins. Eur. J. Mineral. 21, 219–231.

Chen, K.Y., Yuan, H.L., Bao, Z.A., Zong, C.L., Dai, M.N., 2014. Precise and accurate in situ determination of lead isotope ratios in NIST, USGS, MPI-DING and CGSG glass reference materials using femtosecond laser ablation MC-ICP-MS. Geostand. Geoanal. Res. 38, 5–21.

Kind, R., Ni, J., Zhao, W., Wu, J., Yuan, X., Zhao, L., Sandvol, E., Reese, C., Nabelek, J., Hearn, T., 1996. Evidence from earthquake data for a partially molten crustal layer in

Southern Tibet. Science 274, 1692–1694.
Lan, T.G., Hu, R.Z., Fan, H.R., Bi, X.W., Tang, Y.W., Zhou, L., Mao, W., Chen, Y.H., 2017. In-situ analysis of major and trace elements in fluid inclusion and quartz: LA-ICP-MS method and applications to ore deposits. Acta Petrol. Sin. 33, 3239–3262 (in Chinese with English abstract).
Lan, T.G., Hu, R.Z., Bi, X.W., Mao, G.J., Wen, B.J., Liu, L., Chen, Y.H., 2018. Metasomatized asthenospheric mantle contributing to the generation of Cu-Mo deposits within an intracontinental setting: a case study of the ~128 Ma Wangjiazhuang Cu-Mo deposit, eastern North China Craton. J. Asian Earth Sci. 160, 460–489.
Landtwing, M.R., Pettke, T., 2005. Relationships between SEM-cathodoluminescence response and trace-element composition of hydrothermal vein quartz. Am. Mineral. 90, 122–131.
Large, R.R., Bull, S.W., Winefield, P.R., 2001. Carbon and oxygen isotope halo in carbonates related to the McArthur River (HYC) Zn-Pb-Ag deposit, North Australia: implications for sedimentation, ore genesis, and mineral exploration. Econ. Geol. 96, 1567–1593.
Levresse, G., González-Partida, E., Carrillo-Chavez, A., Tritlla, J., Camprubí, A., Cheilletz, A., Gasquet, D., Deloule, E., 2004. Petrology, U/Pb dating and (C-O) stable isotope constraints on the source and evolution of the adakite-related Mezcala Fe-Au skarn district, Guerrero. Mexico. Miner. Deposita 39, 301–312.
Liu, X.J., 2008. Ore-forming environment and genesis of Leqingla lead-zinc deposit, Tibet. Master Thesis (in Chinese with English abstract). China University of Geosciences, Beijing, pp. 1–74.
Liu, Y., Fan, Y., Zhou, T.F., Xiao, X., White, N.C., Thompson, J., Hong, H.L., Zhang, L.J., 2019. Geochemical characteristics of magnetite in Longqiao skarn iron deposit in the Middle-Lower Yangtze Metallogenic Belt, Eastern China. Miner. Deposita.
Liu, Y.S., Hu, Z.C., Gao, S., Günther, D., Xu, J., Gao, C.G., Chen, H.H., 2008. In situ analysis of major and trace elements of anhydrous minerals by LA-ICP-MS without applying an internal standard. Chem. Geol. 257, 34–43.
Luo, K., Zhou, J.X., Huang, Z.L., Caulfield, J., Zhao, J.X., Feng, Y.X., Ouyang, H., 2020. New insights into the evolution of MVT hydrothermal system: A case study of the Wusihe Pb-Zn deposit (South China), using quartz in situ trace elements and sulfides in situ S-Pb isotopes. Am. Mineral. https://doi.org/10.2138/am-2020-7021.
Meinert, L.D., 1992. Skarns and Skarn Deposits. Geosci. Can. 19, 145–162.
Merino, E., Harvey, C., Murray, H.H., 1989. Aqueous-chemical control of the tetrahedral-aluminum content of quartz, halloysite, and other low-temperature silicates. Clays Clay Miner. 37, 135–142.
Mo, X.X., Dong, G.C., Zhao, Z.D., Guo, T.Y., Wang, L.L., Chen, T., 2005. Timing of Magma Mixing in the Gangdisê Magmatic Belt during the India-Asia Collision: Zircon SHRIMP U-Pb Dating. Acta Geol. Sin. Engl. 79, 66–76.
Mo, X.X., Hou, Z.Q., Niu, Y.L., Dong, G.C., Qu, X.M., Zhao, Z.D., Yang, Z.M., 2007. Mantle contributions to crustal thickening during continental collision: Evidence from Cenozoic igneous rocks in southern Tibet. Lithos 96, 225–242.
Nadoll, P., Mauk, J.L., Leveille, R.A., Koenig, A.E., 2015. Geochemistry of magnetite from porphyry Cu and skarn deposits in the southwestern United States. Miner. Deposita 50, 493–515.
Ohmoto, H., 1972. Systematics of sulfur and carbon isotopes in hydrothermal ore deposits. Econ. Geol. 67, 551–578.
O'Neil, J.R., Clayton, R.N., Mayeda, T.K., 1969. Oxygen isotope fractionation in divalent metal carbonates. J. Chem. Phys. 51, 5547–5558.
Pan, G.T., Ding, J., Yao, D.S., Wang, L.Q., 2004. Guidebook of 1: 1,500,000 geologic map of the Qinghai–Xizang (Tibet) plateau and adjacent areas. Cartographic Publishing House, Chengdu, China, pp. 1–148 (in Chinese).
Pan, G.T., Mo, X.X., Hou, Z.Q., Zhu, D.C., Wang, L.Q., Li, G.M., Zhao, Z.D., Geng, Q.R., Liao, Z.L., 2006. Spatial–temporal framework of the Gangdese Orogenic Belt and its evolution. Acta Petrol. Sin. 22, 521–533 (in Chinese with English abstract).
Park, C., Song, Y., Kang, I.M., Shim, J., Chung, D., Park, C.-S., 2017. Metasomatic changes during periodic fluid flux recorded in grandite garnet from the Weondong W-skarn deposit, South Korea. Chem. Geol. 451, 135–153.
Pass, H.E., Cooke, D.R., Davidson, G., Maas, R., Dipple, G., Rees, C., Ferreira, L., Taylor, C., Deyell, C.L., 2014. Isotope geochemistry of the Northeast Zone, Mount Polley Alkalic Cu-Au-Ag porphyry deposit, British Columbia: a case for carbonate assimilation. Econ. Geol. 109, 859–890.
Perny, B., Eberhardt, P., Ramseyer, K., Mullis, J., Pankrath, R., 1992. Microdistribution of Al, Li, and Na in α quartz: Possible causes and correlation with short-lived cathodoluminescence. Am. Mineral. 77, 534–544.
Pili, É., Poitrasson, F., Gratier, J.P., 2002. Carbon–oxygen isotope and trace element constraints on how fluids percolate faulted limestones from the San Andreas Fault system: partitioning of fluid sources and pathways. Chem. Geol. 190, 231–250.
Royden, L.H., 1993. The tectonic expression of slab pull of continental convergent boundaries. Tectonics 12, 303–325.
Rusk, B., Koenig, A., Lowers, H., 2011. Visualizing trace element distribution in quartz using cathodoluminescence, electron microprobe, and laser ablation-inductively coupled plasma-mass spectrometry. Am. Mineral. 96, 703–708.
Rusk, B.G., Lowers, H.A., Reed, M.H., 2008. Trace elements in hydrothermal quartz: Relationships to cathodoluminescent textures and insights into vein formation. Geology 36, 547–550.
Rusk, B.G., Reed, M.H., Dilles, J.H., Kent, A.J.R., 2006. Intensity of quartz cathodoluminescence and trace-element content in quartz from the porphyry copper deposit at Butte, Montana. Am. Mineral. 91, 1300–1312.
Sun, G.T., Zeng, Q.D., Wang, Y.B., Li, B., Chen, P.W., 2019. Geochronology and geochemistry of Mesozoic dykes in the Qingchengzi ore field, Liaoning Province, China: Magmatic evolution and implications for ore genesis. Geol. J. https://doi.org/10.1002/gj.3646. gj.3646.
Sun, X., Lu, Y.J., McCuaig, T.C., Zheng, Y.Y., Chang, H.F., Guo, F., Xu, L.J., 2018. Miocene ultrapotassic, high-Mg dioritic, and adakite-like rocks from Zhunuo in Southern Tibet: implications for mantle metasomatism and porphyry copper mineralization in collisional orogens. J. Petrol. 59, 341–386.
Sun, X., Zheng, Y.Y., Xu, J., Huang, L.H., Guo, F., Gao, S.B., 2017. Metallogenesis and ore controls of Cenozoic porphyry Mo deposits in the Gangdese belt of southern Tibet. Ore Geol. Rev. 81, 996–1014.
Tang, J.X., Li, F., Li, Z., Zhang, L., Deng, Q., Lang, X., Huang, Y., Yao, X., Wang, Y., 2010. Time limit for formation of main geological bodies in Xiongcun copper–gold deposit, Xietongmen County, Tibet: evidence from zircon U-Pb ages and Re–Os age of molybdenite. Miner. Depos. 29, 461–475 (in Chinese with English abstract).
Tanner, D., Henley, R.W., Mavrogenes, J.A., Holden, P., 2013. Combining in situ isotopic, trace element and textural analyses of quartz from four magmatic-hydrothermal ore deposits. Contrib. Mineral. Petrol. 166, 1119–1142.
Taylor, H.P., 1974. The application of oxygen and hydrogen isotope studies to problems of hydrothermal alteration and ore deposition. Econ. Geol. 69, 843–883.
Taylor, H.P., Frechen, J., Degens, E.T., 1967. Oxygen and carbon isotope studies of carbonatites from the Laacher See District, West Germany and the Alnö District, Sweden. Geochim. Cosmochim. Acta 31, 407–430.
Vazquez, R., Vennemann, T.W., Kesler, S.E., Russell, N., 1998. Carbon and oxygen isotope halos in the host limestone, El Mochito Zn-Pb-(Ag) skarn massive sulfide-oxide deposit, Honduras. Econ. Geol. 93, 15–31.
Wang, L.Q., 2010. Geological, geochemical characteristics and genesis of the Mengya'a lead-zinc deposit, Tibet. Master Thesis (in Chinese with English abstract). China University of Geosciences, Beijing, pp. 1–50.
Wang, L.Q., Cheng, W.B., Tang, J.X., Kang, H.R., Zhang, Y., Li, Z., 2016. U-Pb geochronology, geochemistry, and H–O–S–Pb isotopic compositions of the Leqingla and Xin'gaguo skarn Pb–Zn polymetallic deposits, Tibet, China. J. Asian Earth Sci. 115, 80–96.
Wang, L.Q., Tang, J.X., Deng, J., Kang, H.R., Lin, X., Cheng, W.B., Li, Z., Zhang, Z., 2015. The Longmala and Mengya'a skarn Pb–Zn deposits, Gangdese region, Tibet: evidence from U-Pb and Re–Os geochronology for formation during early India-Asia collision. Int. Geol. Rev. 57, 1825–1842.
Wark, D.A., Watson, E.B., 2006. TitaniQ: a titanium-in-quartz geothermometer. Contrib. Mineral. Petrol. 152, 743–754.
Williams, H., Turner, S., Kelley, S., Harris, N., 2001. Age and composition of dikes in Southern Tibet: new constraints on the timing of east-west extension and its relationship to postcollisional volcanism. Geology 29, 339–342.
Wu, F.Y., Yang, J.H., Xu, Y.G., Wilde, S.A., Walker, R.J., 2019. Destruction of the North China Craton in the Mesozoic. Annu. Rev. Earth Pl. Sc. 47, 173–195.
Xiao, X., Zhou, T.F., White, N.C., Zhang, L.J., Fan, Y., Wang, F.Y., Chen, X.F., 2018. The formation and trace elements of garnet in the skarn zone from the Xinqiao Cu-S-Fe-Au deposit, Tongling ore district, Anhui Province, Eastern China. Lithos 302–303, 467–479.
Yang, Z.M., Hou, Z.Q., Chang, Z.S., Li, Q.Y., Liu, Y.F., Qu, H.C., Sun, M.Y., Xu, B., 2016. Cospatial Eocene and Miocene granitoids from the Jiru Cu deposit in Tibet: Petrogenesis and implications for the formation of collisional and postcollisional porphyry Cu systems in continental collision zones. Lithos 245, 243–257.
Yin, A., Harrison, T.M., 2000. Geologic evolution of the Himalayan-Tibetan Orogen. Annu. Rev. Earth. Pl. Sc. 28, 211–280.
Zartman, R.E., Doe, B.R., 1981. Plumbotectonics—the model. Tectonophysics 75, 135–162.
Zeng, Y.C., Chen, J.L., Xu, J.F., Lei, M., Xiong, Q.W., 2017. Origin of Miocene Cu-bearing porphyries in the Zhunuo region of the southern Lhasa subterrane: Constraints from geochronology and geochemistry. Gondwana Res. 41, 51–64.
Zhai, D.G., Liu, J.J., Zhang, H.Y., Wang, J.P., Su, L., Yang, X.A., Wu, S.H., 2014. Origin of oscillatory zoned garnets from the Xieertala Fe–Zn skarn deposit, northern China: In situ LA–ICP-MS evidence. Lithos 190–191, 279–291.
Zhang, L.K., Fan, W.Y., Gao, D.F., 2008. Geology and genesis of Leqingla Pb–Zn polymetallic deposit in the Linzhou County, Tibet. Geol. Prospect. 44, 10–16 (in Chinese with English abstract).
Zhang, Z.M., Dong, X., Santosh, M., Liu, F., Wang, W., Yiu, F., He, Z.Y., Shen, K., 2012. Petrology and geochronology of the Namche Barwa Complex in the eastern Himalayan syntaxis, Tibet: Constraints on the origin and evolution of the northeastern margin of the Indian Craton. Gondwana Res. 21, 123–137.
Zhang, Z.M., Dong, X., Santosh, M., Zhao, G.C., 2014. Metamorphism and tectonic evolution of the Lhasa terrane, Central Tibet. Gondwana Res. 25, 170–189.
Zhao, J.X., Li, G.M., Evans, N.J., Qin, K.Z., Li, J.X., Zhang, X.N., 2016. Petrogenesis of Paleocene-Eocene porphyry deposit-related granitic rocks in the Yaguila-Sharang ore district, central Lhasa terrane, Tibet. J. Asian Earth Sci. 129, 38–53.
Zhao, J.X., Qin, K.Z., Li, G.M., Cao, M.J., Evans, N.J., McInnes, B.I.A., Li, J.X., Xiao, B., Chen, L., 2015. The exhumation history of collision-related mineralizing systems in Tibet: Insights from thermal studies of the Sharang and Yaguila deposits, central Lhasa. Ore Geol. Rev. 65, 1043–1061.
Zhao, J.X., Qin, K.Z., Li, G.M., Li, J.X., Xiao, B., Chen, L., Yang, Y.H., Li, C., Liu, Y.S., 2014. Collision-related genesis of the Sharang porphyry molybdenum deposit, Tibet: Evidence from zircon U-Pb ages, Re-Os ages and Lu-Hf isotopes. Ore Geol. Rev. 56, 312–326.
Zhao, W.W., Zhou, M.-F., 2015. In-situ LA-ICP-MS trace elemental analyses of magnetite: The Mesozoic Tengtie skarn Fe deposit in the Nanling Range, South China. Ore Geol. Rev. 65, 872–883.
Zheng, J.P., Dai, H.K., 2018. Subduction and retreating of the western Pacific plate resulted in lithospheric mantle replacement and coupled basin-mountain respond in the North China Craton. Sci. China Earth Sci. 61, 406–424.
Zheng, Y.C., Fu, Q., Hou, Z.Q., Yang, Z.S., Huang, K.X., Wu, C.D., Sun, Q.Z., 2015. Metallogeny of the northeastern Gangdese Pb–Zn–Ag–Fe–Mo–W polymetallic belt in the Lhasa terrane, southern Tibet. Ore Geol. Rev. 70, 510–532.
Zheng, Y.F., Hoefs, J., 1993. Carbon and oxygen isotopic covariations in hydrothermal

calcites. Mineral. Deposita 28, 79–89.
Zhou, J.H., Feng, C.Y., Li, D.X., 2017. Geochemistry of the garnets in the Baiganhu W-Sn orefield, NW China. Ore Geol. Rev. 82, 70–92.
Zhou, J.X., Bai, J.H., Huang, Z.L., Zhu, D., Yan, Z.F., Lv, Z.C., 2015. Geology, isotope geochemistry and geochronology of the Jinshachang carbonate-hosted Pb-Zn deposit, southwest China. J. Asian Earth Sci. 98, 272–284.
Zhou, J.X., Luo, K., Li, B., Huang, Z.L., Yan, Z.F., 2016. Geological and isotopic constraints on the origin of the Anle carbonate-hosted Zn-Pb deposit in northwestern Yunnan Province, SW China. Ore Geol. Rev. 74, 88–100.
Zhou, J.X., Luo, K., Wang, X.C., Wilde, S.A., Wu, T., Huang, Z.L., Cui, Y.L., Zhao, J.X., 2018a. Ore genesis of the Fule PbZn deposit and its relationship with the Emeishan Large Igneous Province: Evidence from mineralogy, bulk C-O-S and in situ S-Pb isotopes. Gondwana Res. 54, 161–179.
Zhou, J.X., Xiang, Z.Z., Zhou, M.F., Feng, Y.X., Luo, K., Huang, Z.L., Wu, T., 2018b. The giant Upper Yangtze Pb-Zn province in SW China: Reviews, new advances and a new genetic model. J. Asian Earth Sci. 154, 280–315.
Zhou, J.X., Wang, X.C., Wilde, S.A., Luo, K., Huang, Z.L., Wu, T., Jin, Z.G., 2018c. New insights into the metallogeny of MVT Zn-Pb deposits: A case study from the Nayongzhi in South China, using field data, fluid compositions, and in situ S-Pb isotopes. Am. Mineral. 103, 91–108.
Zhu, D.C., Mo, X.X., Zhao, Z.D., Niu, Y., Wang, L.Q., Chu, Q.H., Pan, G.T., Xu, J.F., Zhou, C.Y., 2010. Presence of Permian extension- and arc-type magmatism in southern Tibet: Paleogeographic implications. GSA Bull. 122, 979–993.
Zhu, D.C., Zhao, Z.D., Niu, Y., Dilek, Y., Hou, Z.Q., Mo, X.X., 2013. The origin and pre-Cenozoic evolution of the Tibetan Plateau. Gondwana Res. 23, 1429–1454.
Zhu, D.C., Zhao, Z.D., Niu, Y., Mo, X.X., Chung, S.L., Hou, Z.Q., Wang, L.Q., Wu, F.Y., 2011. The Lhasa Terrane: Record of a microcontinent and its histories of drift and growth. Earth Planet. Sci. Lett. 301, 241–255.
Zhu, D.C., Zhao, Z.D., Pan, G.T., Lee, H.Y., Kang, Z.Q., Liao, Z.L., Wang, L.Q., Li, G.M., Dong, G.C., Liu, B., 2009. Early cretaceous subduction-related adakite-like rocks of the Gangdese Belt, southern Tibet: Products of slab melting and subsequent melt–peridotite interaction? J. Asian Earth Sci. 34, 298–309.